POLITECNICO DI MILANO
DEPARTMENT OF AEROSPACE SCIENCE AND TECHNOLOGY
DOCTORAL PROGRAMME IN AEROSPACE ENGINEERING

INVESTIGATION ON THE HELICOPTER/OBSTACLE AERODYNAMIC INTERACTION

Doctoral Dissertation of:
Daniele Zagaglia

Supervisor:
Prof. Giuseppe Gibertini

Tutor:
Prof. Luigi Vigevano

The Chair of the Doctoral Program:
Prof. Luigi Vigevano

2017 – Cycle XXIX

Acknowledgements

Firstly, I would like to express my sincere gratitude to my advisor Prof. Giuseppe Gibertini, for the continuous support of my Ph.D. study and related research, for his patience, motivation, and invaluable advices.

Besides my advisor, I would like to thank Prof. Richard Green for giving me the opportunity of spending part of my Ph.D. at the University of Glasgow and allowing me to take advantage of its experimental resources. My sincere gratitude goes to Dr. Michea Giuni as well, who unceasingly and patiently helped me during my period abroad.

I would also like to thank Prof. Markus Raffel and Prof. Gaetano Iuso for making themselves available to review the present Ph.D dissertation.

Coming back to Milan, I would like to express my gratitude to Donato Grassi and Gabriele Campanardi, whose contribution in setting up the experimental setup has been invaluable.

Many thanks as well to my fellow officemates Alex Zanotti (or Prof. Zanotti by now), Giovanni Droandi, Davide Montagnani, Federico Fonte, Luca Riccobene, Alessandro De Gaspari and Matteo Tugnoli for the stimulating discussions, for their invaluable help and advise, and for all the fun we have had in the last three years, making the office a space worth spending time in.

I also want to thank all my friends, especially the *Banda* members, for giving me support, for making me smile in my good and bad times, and for helping me cope with the stress that the challenging profession I have chosen unavoidably entails.

Last but not the least, I would like to thank my family: especially my parents and my brother Alessandro for supporting me spiritually throughout writing this thesis and my life in general. I owe you everything.

Abstract

THE helicopter is a very versatile flying machine which is often required to operate within confined areas, due to its capability of managing hovering flight. The aerodynamic interaction that develops between the rotor-induced wake and the surrounding obstacles typically generates, on the one hand, a degradation of the helicopter performance and high compensatory workload for the pilot, on the other hand unsteady forces which can stress the structure of the surrounding obstacles. Despite the presence of a fair number of numerical and experimental investigations on this topic, a systematic study of these aerodynamic phenomena in order to disclose the key aerodynamic mechanisms of this interaction is still lacking. In the present work, a comprehensive experimental survey for the investigation of the aerodynamic interference between a model ground obstacle and a helicopter hovering in its proximity is described. The effect of the presence of external wind was also taken in consideration at a later stage. The experimental activities were carried out at Politecnico di Milano and University of Glasgow and took advantage of several rotor rigs and experimental techniques. Load measurements on the rotor were carried out in order to assess the rotor performance for different rotor positions with respect to the obstacle. Laser Doppler Anemometry (LDA) measurements of the rotor inflow were used in order to see how the aerodynamic interaction affected the rotor performance. Particle Image Velocimetry (PIV) measurements in the region between the rotor and the obstacle were carried out in order to have a better insight of the interacting flow field. Steady and unsteady pressure measurements on the obstacle allowed a better understanding of how the interactional phenomena affected the loading on the surrounding structures.

Sommario

L'ELICOTTERO è una macchina volante che spesso è utilizzata in ambienti confinati, vista la sua capacità di volare a punto fisso. L'interazione aerodinamica che si sviluppa tra la scia rilasciata dal rotore e gli ostacoli circostanti genera tipicamente, da un lato, un peggioramento delle prestazioni dell'elicottero ed un aumento del lavoro di compensazione del pilota, dall'altro lato carichi instazionari che colpiscono le strutture circostanti. Nonostante la presenza di un buon numero di indagini sperimentali e numeriche sull'argomento, uno studio sistematico è tuttora mancante, che possa svelare i meccanismi fluidodinamici chiave di questo tipo di interazione. Nel seguente lavoro sono quindi descritti i risulati di un indagine sperimentale sull'interferenza aerodinamica tra un elicottero ed un prototipo semplificato di ostacolo, tenendo conto in un secondo momento anche degli effetti del vento. Le attività sperimentali sono state svolte al Politecnico di Milano e all'Università di Glasgow, utilizzando più apparati sperimentali ed utilizzando diverse tecniche di misura. Sono state effettuate misure delle forze e momenti agenti sul rotore in modo da valutare le prestazioni dello stesso per diverse posizioni rispetto all'ostacolo. Sono state svolte misure dell'inflow del rotore tramite anemometria laser-doppler (LDA) per vedere come i fenomeni interazionali agissero sull'aerodinamica del rotore, mentre il campo di moto tra il rotore e l'ostacolo è stato indagato tramite velocimetria ad immagini di particelle (PIV). Infine, per analizzare i carichi instazionari agenti sull'ostacolo, misure di pressione mediate e non sono state realizzate sul modello di edificio.

Contents

List of Symbols and Acronyms

List of symbols

A	=	rotor disk area, m, πR^2
c	=	Blade chord, m
c_∞	=	Asymptotic speed of sound, m/s
c_{Mx}, c_{My}	=	Rotor in-plane moment coefficients, $M_x/(\rho V_{TIP}^2 AR)$
c_P	=	Pressure coefficient based on the induced velocity, $(P - P_\infty)/(1/2\rho V_{IND}^2)$
c_P^*	=	Pressure coefficient based on free-stream velocity, $(P - P_\infty)/(1/2\rho U_\infty^2)$
c_Q	=	Rotor torque coefficient, $Q/(\rho V_{TIP}^2 AR)$
c_T	=	Rotor thrust coefficient, $T/(\rho V_{TIP}^2 A)$
D	=	Rotor diameter, m
f	=	frequency, Hz
$\|F(*)\|$	=	Amplitude of the Fourier Transform of variable *, Hz
FM	=	Figure of Merit, $C_T/(C_Q^{3/2}\sqrt{2})$
M	=	PIV optical magnification factor, pixels/mm
M_{TIP}	=	Mach number at Blade tip, V_{TIP}/c_∞
P	=	Local pressure, Pa
P_∞	=	Free-stream reference pressure, Pa
Q	=	Rotor torque, Nm
R	=	Rotor radius, m
Re_{TIP}	=	Reynolds number at Blade tip, $V_{TIP}c/\nu$
T	=	Rotor thrust, Nm
U_∞	=	Free-stream velocity
V_{TIP}	=	Blade tip velocity, ΩR
V_{IND}	=	Rotor induced velocity according to momentum theory, m/s

(X, Y, Z)	=	Absolute reference System
(x, y, z)	=	Rotor reference System
Δt	=	Laser pulse delay time , μs
ν	=	Fluid cinematic viscosity, m^2/s
ρ	=	Air density, kg/m^3
ϵ_{c_T}	=	Uncertainty on the Thrust coefficient
ϵ_{c_P}	=	Uncertainty on the Pressure coefficient
ϵ_u	=	Uncertainty on the PIV velocity field, in-plane velocity components, m/s
$\epsilon_{u,op}$	=	Uncertainty on the PIV velocity field, out-of-plane velocity components, m/s
μ	=	Advance Ratio, U_∞ / V_{TIP}
θ	=	Half camera separation angle
Ω	=	Rotational frequency of the rotor, rpm

Acronyms

AG22	=	GARTEUR Action Group 22
CIRA	=	Centro Italiano Ricerche Aerospaziali, Italian Aerospace Centre
CFD	=	Computational Fluid Dynamics
DI	=	Dynamic Interface
DLR	=	Deutsches Zentrum fur Luft- und Raumfahrt, German Aerospace Centre
GARTEUR	=	Group for Aeronautical Research and Technology in EURope
GVPM	=	Galleria del Vento Politecnico di Milano
IHST	=	International Helicopter Safety Team
IGE	=	In Ground Effect
JHSAT	=	Joint Helicopter Safety Analysis Team
LDA	=	Laser Doppler Anemometry
NLR	=	Nederlands Lucht- en Ruimtevaartcentrum, Dutch Aerospace Centre
OGE	=	Out of Ground Effect
ONERA	=	Office National d'Etudes et de Recherches Aerospatiales, French Aerospace Centre
POLIMI	=	Politecnico di Milano
PIV	=	Particle Image Velocimetry
RPM	=	Revolutions Per Minute

CHAPTER 1

Introduction

In this chapter, the problem of the helicopter/obstacle aerodynamic interaction is firstly introduced in section 1.1. The state of the art for both the experimental (Section 1.2) and numerical (Section 1.3) investigations is then discussed. The motivation and the purpose of the present thesis word are described in section 1.4. Eventually the thesis layout and the content of each chapter are illustrated in section 1.5.

1.1 The problem

The helicopter is a very versatile flying machine which is often required to operate within confined areas, due to its capability of managing hovering flight. These challenging operational areas comprise naval environments, e.g. the landing manoeuvre on a helicopter carrier, and rescue operations in confined areas and urban environments where the helicopter interacts with the surrounding buildings, the so-called city canyoning. A few of these operational environments are presented in Figure 1.1.

The aerodynamic interaction between the rotor-induced wake and the surrounding obstacles, such as buildings and mountain walls, typically generates, on the one hand, a degradation of the helicopter performance and high compensatory workload for the pilot [1], on the other hand unsteady forces which can stress the structure of the surrounding obstacles. Important issues of noise may also arise which

(a) *Urban environments*

(b) *Search and rescue missions*

(c) *Offshore platforms*

(d) *Ship decks*

Figure 1.1: *Examples of helicopters operating in confined environments*

have the potential to create discomfort to the community residing in the proximity of the area. This situation can be further complicated by the presence of wind, since the helicopter has to interact with the highly unstaeady and turbulent wake generated by the obstacle.

The danger intrinsic to these flight conditions is evident in the accident database [2] collected by the Joint Helicopter Safety Analysis Team (JHSAT) for the International Helicopter Safety Team (IHST), which is a team of government and industry leaders whose mission is to establish international partnerships in countries with significant helicopter operations and encourage development and implementation of safety interventions by sharing lessons learned through accident analysis. The so gathered database analyses 523 helicopter accidents occurred in the United States of America in 2000, 2001 and 2006, sorting them in terms of flight phase, occurrence category and motivation. This study highlighted that most of the helicopter accidents (61.4 %) occur during take-off and landing, hence generally in the presence of ground obstacles. Among these accidents, 7.5% resulted in human casualties. In particular, 41% of the total number of accidents were accounted for pilot performance management issues, i.e. the fact that the pilot was not capable of contrast the change in the helicopter performance due to external perturbations.

1.2 Experimental Investigations: State of the Art

Interactional aerodynamics, i.e. the study of the flow anomalies and the associated forces that result from combining the active (rotor) and passive (fuselage, obstacles, etc.) components of an helicopter configuration, has been an important research topic in the rotorcraft community since the early '80s (Sheridan and Smith, [3]). The rotor-fuselage interference has been thoroughly investigated (e.g. [4], [5], [6]) and most of the issues related to this problem have been solved.

However the helicopter interaction with ground obstacle is a somehow more complex matter, since the relative distance between the active and passive component is not fixed as in the helicopter-fuselage case, but it changes according to the helicopter relative movements with respect to the obstacle, originating a serie of various aerodynamic phenomena.

The number of experimental studies regarding the interaction with simplified basilar geometries (i.e. semi-infinite vertical walls, parallelepipeds, etc.) is unexpectedly small with respect to those comprising more complex geometries. Among these, Timm in [7] was the first to observe the flow recirculation induced by the interaction between the rotor and obstacle through flow visualisations. Iboshi et al. investigated in [8] the ground effect of a fully articulated rotor in ground effect above a confined area between two vertical walls, finding that the re-circulatory flow upward along the wall causes both the steady and vibratory torque coefficients to increase. The effect is either a downwash or up-wash based on the combinations of the wall height, the space between walls, and the rotor height.

For what concerns the helicopter interaction with more complex geometries, the Dynamic Interface problem [9], i.e. the launch and recovery of flight vehicles, primarily rotorcrafts, onto ships in windy conditions, is probably the most investigated configuration from both the experimental and numerical point of view.

On this topic, one of the first experimental works was produced by Zan in [10], where he presented the experimental measurements of time-averaged rotor thrust coefficients for a rotor immersed the airwake of the Canadian Patrol Frigate ship. The author shows how the interaction can significantly decrease rotor thrust up to 10% to 15%, thereby impacting operational envelopes. Zan proposed a set of changes in the ship superstructure geometry which were able to reduce the severity of the airwake and also lessen the spatial gradients of the rotor thrust coefficient. Further studies allowed to investigate also the unsteady loads on the fuselage immersed in the ship wake (Lee and Zan, [11]) and the full configuration comprising rotor and fuselage (Lee and Zan [12]).

Another test rig for the investigation of the helicopter loads in a ship's airwake was developed by Kääriä et al. in [13] and [14]. In particular experiments were conducted in a water tunnel using a specially designed Airwake Dynamometer (AirDyn) to characterise the aerodynamic loading of the helicopter immersed in the ship-wake, showing very strong variation of both the average and unsteady loads due to the strong velocity gradients that develop in the wake of the ship.

The experimental investigations found in the literature do not only focus on the change in the rotor performance, but they also focus on other kind of flow measurements (however seldom in the same paper). As an example, Quinliven at al. [15] investigated the inflow region and the wake of a rotor in proximity of a building model, highlighting the effect of the flow-recirculation that occurs when the rotor is close to the building.

Another kind of measurement was adopted by Rajagopalan et al in [16], where Particle Image Velocimetry (PIV) was used to acquire 3-component velocity field measurements of the combined wake of a tandem-rotor helicopter and a ship. PIV was also used by Nacakli and Landman in [17] to investigate the recirculation region between a rotor and the vertical wall of a ship deck.

Basic measurements of the downwash and outwash from the rotor of a full-scale helicopter hovering near a land-based hangar were achieved by Polsky and Wilkinson in [18].

As it has been shown, the cited works usually deal with very specific and complex geometries and seldom use more than one measurement technique, focusing either on the rotor performance or the flowfield measurements. Moreover the effect of the helicopter on the obstacle was never investigated.

1.3 Numerical Investigations: State of the Art

As for the experimental investigations, the Dynamic Interface problem is probably the most investigated configuration for the numerical simulations as well. In particular, computational fluid dynamics (CFD) simulations of the ship airwakes have been used [1] to improve the realism of flight-simulation software, the so-called frozen airwake approach. CFD-based data of the wind-generated wake are stored and used to modify the local velocity seen by the rotorcraft, in order to estimate the variations in its performance. However this is a one-way coupling since the helicopter does not influence the flow-field, whereas a fully-coupled simulation has been shown to be necessary in order to properly describe these phenomena [19,20].

Several degrees of approximation can be employed for the fully-coupled aerodynamic simulation of the helicopter-obstacle interaction. The most natural and possibly high-fidelity method is to actually solve the flow around each rotating blade. This method allows to capture the time-dependent features of the rotor wake and the aerodynamic interference between the rotor and the obstacle, but it is extremely onerous from a time and computer-memory point of view, thus often making these kind of simulations unaffordable.

A further step of approximation can be achieved by modeling the effect of the rotor on the flow rather than solving the flow around the blades, using the actuator disk method in order to make the numerical simulation less computationally onerous than the previously-described approach. The standard actuator disk model represents the rotor as an infinitely thin disk which carries discontinuities of flow properties, which are dependent on the revolution-averaged disk loading, at the

cost of losing the time-dependent description of the blade passing. This can be generally achieved in two different ways. The first is to directly enforce a pressure jump across the rotor disc as a boundary condition, as it was implemented in [21]. The second possible implementation is through the addition of source terms in the momentum and energy equations in correspondence of the disk plane, as in [22]. The latter method usually results to be more robust, as it was investigated by Le Chuiton in [23].

Once again a further degree of approximation can be introduced, by choosing a closed-loop or open-loop description of the actuator disks. In the open-loop approach the pressure jump on the rotor is imposed *a priori* based on the local disk loading as in [18,19,24], whereas the closed-loop approach updates the rotor inflow according to the computed flow-field, at the cost of a few steady-state iterations, as implemented in [16] by Rajagopalan et al. The inherent time-dependency of the wake structures can be recovered using an unsteady actuator disk or actuator blade model [25, 26], where the momentum source on the disk follow each blade rather than being averaged over a complete revolution.

1.4 Motivation and description of the thesis

Despite the presence of a fair number of numerical and experimental investigations, a systematic study of these aerodynamic phenomena is still lacking. Moreover the past studies usually involve very specific geometries (e.g. ship decks, specific buildings) or focus just on the helicopter performance, neglecting *de facto* the environmental effects that the rotor has on its surroundings.

The idea behind the present work is thus to experimentally investigate this problem, simplifying the obstacle geometry up to a well-defined cubic or parallelepiped shape in order to disclose the key fluid-dynamic mechanisms that occur when a helicopter is hovering in its proximity. Similarly, a rigid unarticulated rotor was adopted, not allowing the flapping and lag blade motion which are quite difficult to be monitored on a small-scale model. In this way, the rotor geometry was *a priori* known and well-defined, while the general wake features were still representative of those of a real rotor.

The interference problem was analysed for several positions of the helicopter model with respect to the obstacle, in order to appreciate how it affects both the rotor performance and the loading on the obstacle itself. The effect of the presence of external wind was also taken in consideration as a following step.

The investigation was carried out through two different test campaigns. The first, carried out at the University of Glasgow, consisted of a set of tests reproducing hovering flight conditions at different positions with respect to a simplified obstacle with a cubic shape, in absence of external wind. This experimental campaign took advantage of several experimental techniques:

- Force and moment measurements on the rotor

- LDA measurements ([27], [28]) of the rotor inflow
- Stereo-PIV ([29], [30]) measurements of the interacting flow-field

The second test campaign was instead carried out at Politecnico di Milano and consisted in the analysis of a helicopter model interacting with a parallelepiped-shaped obstacle in both windy and not-windy conditions. This experimental campaign took advantage of following experimental techniques:

- Force and moment measurements on the rotor
- Steady and unsteady pressure measurements on the obstacle
- PIV measurements of the interacting flow-field

In conclusion, the purpose of the present work is to understand the key aerodynamic mechanisms that occur when an helicopter is hovering in proximity to a well-defined, simplified, obstacle in both windy and not-windy conditions, and to understand how they affect both the helicopter performance and the obstacle.

The work that has been carried out for this thesis will be also be of use for the GARTEUR (see [31]) Action Group 22 *"Forces on Obstacles in Rotor Wake"*. This action group originates from the idea of promoting activities which could contribute to a better understanding of these phenomena and comprises several universities (Politecnico di Milano, University of Glasgow, National Technical university of Athens) and research institutes (CIRA, DLR, ONERA, NLR).

The activities of this GARTEUR action group comprise two sets of activities:

- Experimental investigations of these phenomena, to disclose the main features of the interacting flowfield and its effect on both the helicopter performance and the obstacle. The present work was in the framework of this first set of activities.
- Development of numerical tools capable of predicting the effect of this interference and their validation against the gathered experimental databases.

1.5 Thesis Layout

In this section, a brief overview of the chapter content is addressed, as follows:

In **Chapter 1**, the problem of the helicopter/obstacle aerodynamic interaction has been introduced. The state of the art for both experimental and numerical investigations has been then discussed, giving the motivation and the purpose of the present thesis work. Eventually the thesis layout and the content of each chapter are here illustrated.

In **Chapter 2** the test rigs and the experimental set-ups used during the various test campaigns are described, together with the corresponding test configuration and test points.

In **Chapter 3** the main results of the two experimental campaigns in absence of external wind are presented, basically representing different hovering positions of the helicopter model with respect to the obstacle. Firstly the results of the Glasgow experimental campaign are shown, comprising load and moment measurements on the rotor, LDA measurements of the rotor inflow and Stereo-PIV measurements of the flow-field generated by the interaction. The results of the experimental campaign carried out at Politecnico di Milano are then presented, comprising load and moment measurements on the rotor, unsteady and averaged pressure measurements on the obstacle and PIV measurements of the flow-field. Eventually a few comparisons are drawn between the results obtained in the two experimental campaigns.

In **Chapter 4** the main results for the wind-on experimental campaign carried out at Politecnico di Milano are presented. Firstly a brief description of the flow that develops around a general wall-mounted obstacle is addressed, then the flow around the specific obstacle geometry in absence of the helicopter is investigated. Eventually the results for the helicopter-obstacle interaction test in presence of external wind are presented, compared with those obtained for the wind-off case.

Eventually **Chapter 5** presents the conclusions of the present work.

CHAPTER 2

Test Rigs, Instrumentation and Test Points

In this chapter, the test rigs and the experimental set-ups used during the various test campaigns are described, together with the corresponding test configuration. The two test rigs utilised during the wind-off test campaign at the University of Glasgow are described in section 2.1, whereas the corresponding test points are described in section 2.2. Subsequently the test rig utilised at Politecnico di Milano for the wind-off and wind-on tests is described in section 2.3, followed by its test points in section 2.4.

2.1 Test rig and instrumentation - Glasgow

The experimental campaign that was conducted at the University of Glasgow took advantage of two different rotor rigs, basically representing a rotor interacting with a cubic obstacle whose size was the same of the rotor diameter. The main features of the two rotor rigs are reported in Table 2.1. The two rotor rigs (Figure 2.1) were used for different kind of measurements. In particular the large rotor rig was used for the load measurements and the inflow LDA measurements, whereas the small rotor rig was used to investigate the flow-field by means of Stereoscopic Particle Image Velocimetry (PIV).

The large test rig was placed in a large laboratory space with an even, flat ground extending to a 5m radius away from the rotor centre line, corresponding to 5 rotor diameters.

Characteristics	Symbol	Large rotor rig	Small rotor rig
Cubic Obstacle size	L	1 m	0.3 m
Diameter	D	1 m	0.3 m
Number of blades	N_b	4	2
Blade chord	c	53 mm	31.7 mm
Solidity	σ	0.135	0.134
Collective pitch	θ_c	$8°$	$8°$
Rotor Rotational frequency	Ω	1200 RPM (20 Hz)	4000 RPM (66.6 Hz)
Reynolds Number at blade tip	Re_{TIP}	220000	132000
Mach Number at blade tip	M_{TIP}	0.18	0.18
Type of Experimental investigation		Loads measurement Inflow LDA Measurements	Stereo-PIV

Table 2.1: *Main features of the Rotor Rigs - Glasgow Experimental Campaign*

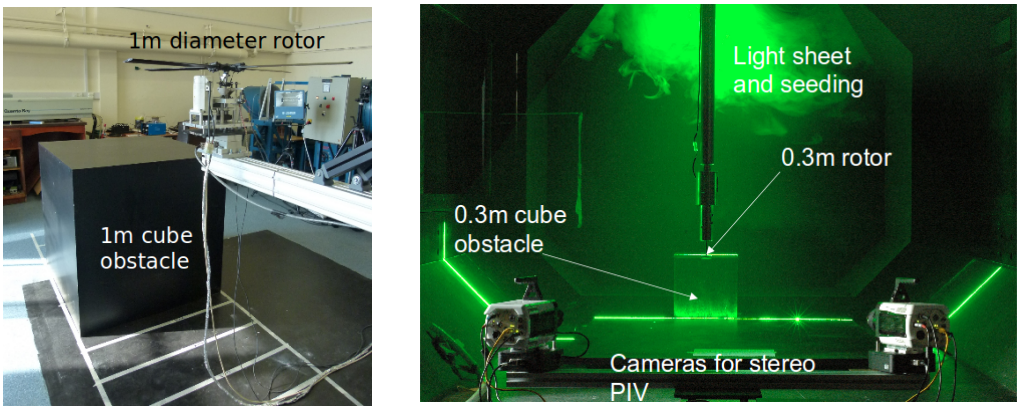

(a) *Glasgow large test rig* **(b)** *Glasgow small rotor rig, with stereo-PIV setup*

Figure 2.1: *Pictures of the Large and Small test rigs - Glasgow experimental campaign*

Two different reference systems are defined, as depicted in Figure 2.2: the global reference system (X, Y, Z) which defines the position of the rotor hub centre with respect to the obstacle and the rotor reference system (x, y, z), which corresponds to the load-cell axes. The origin of the absolute (X, Y, Z) coordinate system is fixed and it is placed on the floor, at the obstacle mid-span.

As previously stated, the large rotor rig was instrumented with a 6-components load cell which allowed the measurements of the forces and moments generated by the rotor. The employed load cell was an AMTI MC36, whose amplifier was set at a very high frequency so that it would respond to the forces and moments. The nominal accuracy of the load cell was 0.25% of the full-scale output, corresponding approximately to 0.5% of the measured thrust in Out of Ground Effect condition. The actual load measurements were obtained as the average of 5 runs, each of which was $2.5\ s$ long. The reduced acquisition time was driven by the need of reducing the load-cell thermal drift.

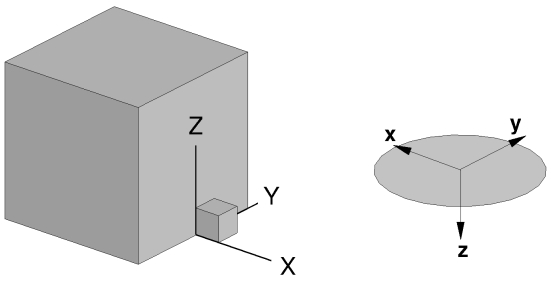

Figure 2.2: *Global* (X, Y, Z) *and Rotor* (x, y, z) *reference systems.*

The rotor inflow measurements were carried out by means of a Dantec 2D Fiber-Flow two-component Laser Doppler Anemometry (LDA) system, in order to understand how the aerodynamic interaction affected the rotor performance. 112 mm probes with beam expanders allowed measurements from over 2000 mm of distance with a measurement volume ellipsoid dimensions of $2.62 \times 0.12 \times 0.12$ mm^3. Seeding was provided by an oil substrate with particle diameter of $0.2 - 0.3$ μm. 7500 valid samples were taken at every measurement point, with accuracy of approximately 0.02 m/s corresponding to 0.4% of the maximum inflow velocity. The LDA system was mounted on a 3D traverse system allowing positioning with accuracy of less than 0.1 mm. The LDA measurements were performed along the rotor x and y axes, 4 cm $(4\%D)$ above the rotor plane, as represented in Figure 2.3. Every LDA sweep comprised 101 evenly-spaced measurement points along the rotor diameter, allowing a spatial resolution of 10 mm $(1\%D)$. The LDA measurements are defined in the rotor reference system (x, y, z). Hence, according to this convention, a positive induced velocity points downwards.

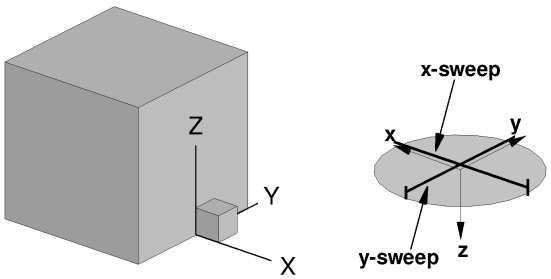

Figure 2.3: *Position of the LDA measurement points along the rotor* x *and* y *axes.*

Stereoscopic PIV was used to investigate the flow in the region between the obstacle and the rotor of the small rotor rig. These measurements were carried out

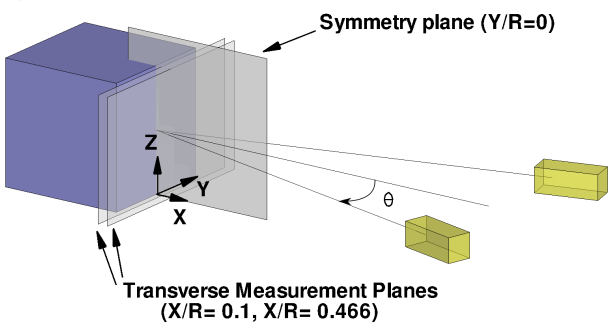

Figure 2.4: *PIV setup and measurement planes - Glasgow experimental campaign*

in the University of Glasgow deHavilland wind tunnel, which has a 2.66m wide x 2.07m high (8.9 $\times$ 7 rotor diameters), by means of a LaVision system running Davis 8. The images were acquired by two Phantom v341 cameras, whose resolution was 4Mpixel. The seeded flow was illuminated by a Nd:YAG laser capable of 100mJ pulses at a maximum repetition rate of 200Hz, thus allowing time resolved measurement of the flow field development to be made. However only the ensemble-averaged measurements over 500 image pairs are addressed in the thesis. The cameras, which were placed on the same or either side of the laser sheet, depending on the investigated plane, were equipped with Scheimpflug adaptors and an angle separation of around 30 degrees was used. Calibration was performed using a 3D calibration plate and Davis 8 software. Oil based seeding for the PIV system was used with nominal particle diameter less than $1\mu m$. The image pairs were post-processed by means of the Davis 8 software using 32×32 pixels interrogation windows with an overlap factor of 50%.

Three measurement planes were investigated, as represented in Figure 2.4:

- The symmetry plane ($Y/R = 0$). In this PIV configuration, the cameras were placed on either side of the laser sheet. The uncertainty of the velocity measurement was estimated (according to [32]) to be $\epsilon_u = \frac{1}{\sqrt{2}}\frac{0.1}{M\Delta t} = 0.1\ m/s$ for the in-plane velocity components and $\epsilon_{u,\text{op}} = \frac{1}{\sqrt{2}\tan\theta}\frac{0.1}{M\Delta t} = 0.33\ m/s$ for the out-of-plane component, assuming a maximum displacement error of 0.1 pixels since a gaussian sub-pixel interpolation algorithm was used. An optical magnification factor of M =3.4161 pixel/mm was obtained through the calibration process, together with a pulse separation time of $\Delta t = 200$ μs and $\theta = 15°$, corresponding to half of the camera separation angle, as represented in Figure 2.4.

- Two transverse planes with different distance from the obstacle, namely $X/R = 0.1$ and $X/R = 0.4666$. In this PIV configuration, the cameras were placed on the same side of the laser sheet. The uncertainty of the velocity measurement was estimated to be $\epsilon_u = 0.07\ m/s$ for the in-plane velocity components

and $\epsilon_{u,\text{op}} = 0.23\ m/s$ for the out-of-plane component, since an optical magnification factor of M =4.85 pixel/mm resulted from the PIV calibration.

An higher camera separation angle could have reduced the out-of-plane versus in-plane velocity error ratio, but unfortunately it was not achievable due to space constraints inside the wind tunnel test section.

2.2 Test Points - Glasgow

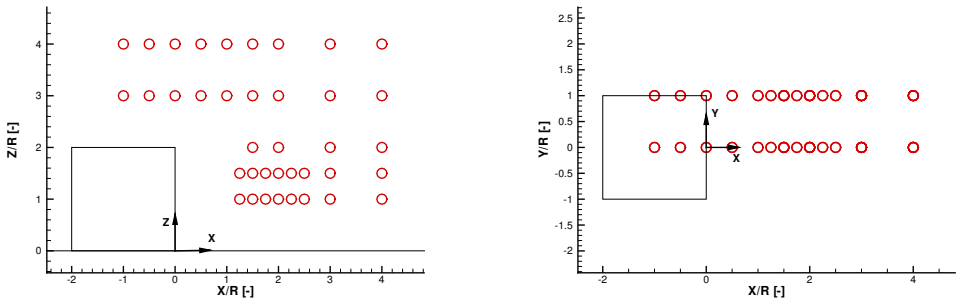

(a) *Test Points - Lateral View - Glasgow Experimental Campaign*

(b) *Test Points - Birdseye View - Glasgow Experimental Campaign*

Figure 2.5: *Test Points. Each point represents the position of the rotor hub centre for that particular Test Point.*

The experimental campaign consisted of a set of tests reproducing hovering flight conditions at several rotor positions with respect to a simplified obstacle with a cubic shape, in absence of external wind.

As previously stated, the data that will be presented in this paper follow the conventions of Figure 2.2. Two different reference systems are defined: the global reference system (X, Y, Z) which defines the position of the rotor hub centre with respect to the obstacle and the rotor reference system (x, y, z), which corresponds to the load-cell axes. The origin of the absolute (X, Y, Z) coordinate system is fixed and it is placed on the floor, at the obstacle mid-span.

The text matrix for the loads measurements is represented in Figure 2.5, where each circle represents the position of the rotor hub centre for that particular test. It consists of several measurement points at the heights of $Z/R = 1, 3/2, 2, 3$ and 4. The measurements were carried out placing the rotor in two different planes:

- $Y/R = 0$, corresponding to the plane symmetry test. The results of this test will be analysed in section 3.1.1.
- $Y/R = 1$, corresponding to the plane coincident to the obstacle lateral face. The results of this test will be analysed in section 3.1.2.

The loads and moments will be expressed according to the rotor reference system (x, y, z). Hence a positive M_y moment is equivalent to a pitching nose-up moment if a helicopter was facing the wall. Similarly, a positive M_x moment is equivalent to a roll moment that promotes a thrust rotation to the left, if a helicopter was facing the obstacle wall.

The LDA measurements were carried out in a subset of the measurement points of figure 2.5, i.e. those at $Z/R = 1.5, 2, 3$, due to the maximum and minimum height achievable by the traversing system. However only the results for $Z/R = 3/2$ and 3 will be shown for the sake of brevity.

The Stereo-PIV measurements were carried out just for the test points at which the rotor was positioned in the symmetry plane, i.e. $Y/R = 0$. In particular the symmetry plane $Y/R = 0$ was investigated for the rotor positions X/R and Z/R varying from $3/2$ to 3, whereas the two transverse planes were acquired just for $X/R = 3/2, Z/R = 2$ and $X/R = 2, Z/R = 2$.

2.3 Test rig and instrumentation - Politecnico di Milano

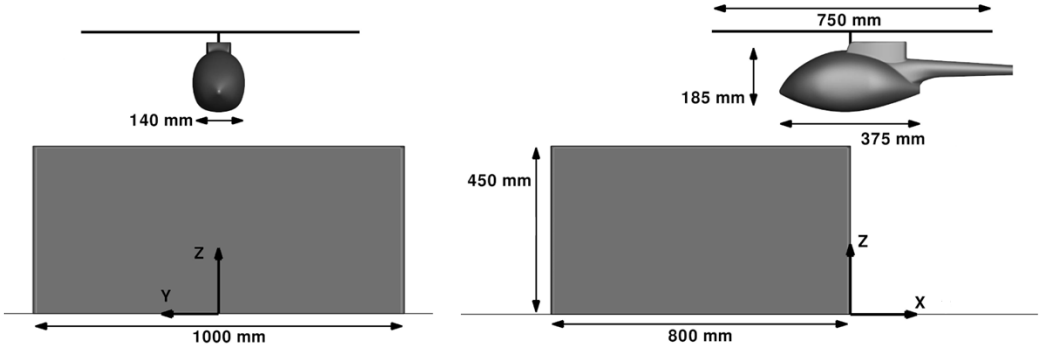

(a) *Test Rig - Frontal View - POLIMI Experimental Campaign*

(b) *Test Rig - Lateral View - POLIMI Experimental Campaign*

Figure 2.6: *The test rig - POLIMI Experimental Campaign.*

The test rig that was used during the test campaign at Politecnico di Milano essentially consisted of a helicopter model, inspired by the MD-500, and a parallelepiped obstacle which represented an ideal building, as represented in Figure 2.6. The helicopter model was held by a horizontal strut fixed to a system of two motorised orthogonal sliding guides to allow the relative position to be changed with respect to the obstacle along the vertical and longitudinal directions of the fuselage. As it can be appreciated, the adopted global reference system (X, Y, Z) is perfectly equivalent to the one previously introduced for the Glasgow experimental campaign. Therefore the X-Z plane is aligned with the mid-span plane of the building model and the X-Y plane is aligned with the floor. The origin of the

reference system is located once again on the floor, at the mid-span of the front face. The rotor reference frame (x, y, z) was equivalent to the one adopted in the Glasgow experimental campaign as well.

The tests were carried out in the large test chamber (suitable for wind engineering tests) of the Large wind tunnel of Politecnico di Milano (GVPM, see ref. [33]), as depicted in Figure 2.8. The test chamber is 13.84 m wide, 3.84 m high and 38 m long. Despite the huge test chamber, a relatively small model was used in order to prevent any interference effect with the surrounding walls. A schematic of the rotor and obstacle models inside the test chamber is depicted in Figure 2.7. The rotor rig features and the test operating condition are summed up in Table 2.2, where also the data for the Glasgow experimental campaign are reported for comparison.

Figure 2.7: *The rotor-obstacle test rig mounted inside the GVPM wind tunnel*

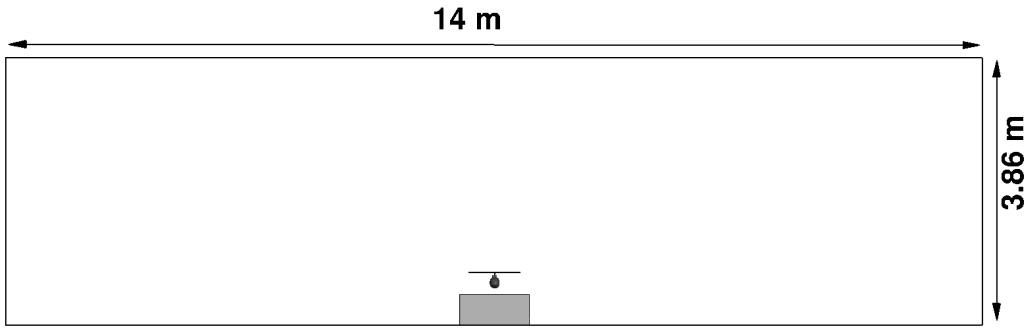

Figure 2.8: *Schematic of the helicopter-obstacle test rig mounted inside the GVPM wind tunnel and test section dimensions.*

Characteristics	POLIMI	Glasgow Large rig	Glasgow Small rig
Obstacle size	1m $\times$ 0.8m $\times$ 0.45m	1m $\times$ 1m $\times$ 1m	0.3m $\times$ 0.3m $\times$ 0.3m
Fuselage	Present	Not Present	Not Present
Rotor Diameter	0.75 m	1 m	0.3 m
Number of blades	4	4	2
Blade chord	32 mm	53 mm	31.7 mm
Solidity	0.11	0.135	0.134
Collective pitch	$10°$	$8°$	$8°$
Rotor Rotational frequency	2580 RPM (43 Hz)	1200 RPM (20 Hz)	4000 RPM (66.6 Hz)
Reynolds Num. at blade tip	220000	220000	132000
Mach Num. at blade tip	0.30	0.18	0.18
Type of Experiment	Loads meas. Pressure meas. 2D-PIV	Loads meas. LDA	Stereo-PIV

Table 2.2: *Main features of the Rotor Rigs*

Figure 2.9a shows a schematic of the helicopter model. The rotor had four untwisted and untapered rectangular blades with a chord of c = 0.032 m and radius of R = 0.375 m. The NACA 0012 airfoil was used. No swash plate was present, so the blade pitch angle was fixed to $10°$. This obviously prevents the possibility of trimming the rotor to a set thrust coefficient or to null pitch and roll moment. Nevertheless the rotor trim has probably scarce influence on the key phenomena that occur in the interaction and, from a dual point of view, by analysing the differences in the forces and moments generated in the different positions by operating the rotor at fixed conditions, one has the indication of the kind of interventions the pilot might have to implement in order to counteract to those variations.

A rotational speed of approximately 2580 rpm was maintained during all the tests by means of a brush-less low-voltage electrical motor with an electronic controller. The resulting Mach number and Reynolds number at the blade tip were $M_{\text{TIP}} = 0.30$ and $Re_{\text{TIP}} = 220,000$, respectively.

A brief discussion on the inexact matching of the Mach and Reynolds number with respect to a real case is in order. As previously stated, the aim of the present study is to analyse the interaction between the rotor wake and obstacle; therefore, matching Mach number at tip was not essential, because the topology of the wake is not greatly influenced by the compressibility effects ([34], [35]). A larger effect of the small-scale can be expected because of the low Re_{TIP}. Depending on the Reynolds numbers, the blade profile drag coefficient varies; this produces a different resistant torque, which translates in a different wake swirl than in full-scale condition. However we must highlight the fact that in the present investigation the employed models were able to reach a Reynolds number higher than most of the other in similar investigations (i.e. [15] and [36]).

The forces and moments acting on the rotor were measured with a six-component balance nested inside the fuselage. A Hall effect sensor produced one signal per revolution to act as the feedback signal for RPM control. According to the nomi-

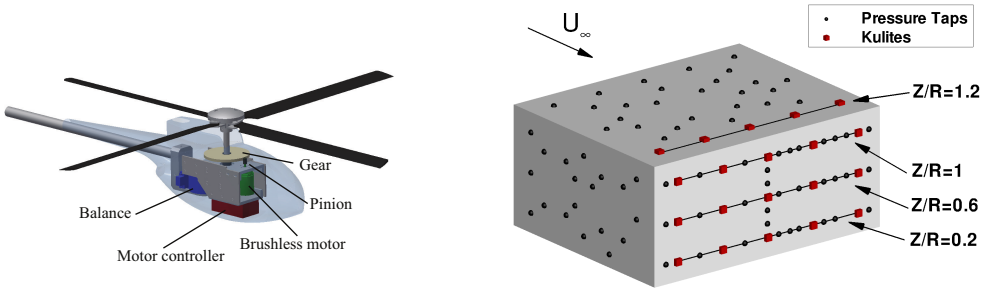

(a) *Layout of the helicopter model and nested instrumentation*

(b) *Obstacle model: location of the pressure taps.*

Figure 2.9: *Schematic of the helicopter and obstacle models, with embedded instrumentation.*

nal accuracy of the whole adopted instrumentation, the uncertainty on the measured thrust coefficient ϵ_{c_T} resulted to be 0.4 % of the Out of Ground Effect (OGE) value, while the uncertainty on the torque and pitch/roll moments resulted to be 0.48 % of the OGE torque coefficient. A repeatability test over 30 realisations of the Out of Ground effect condition ($Z/R = 4$ in absence of the obstacle) exhibited a standard deviation of the thrust and torque coefficients equal to 0.31 % and 0.34 % respectively.

The building model was a parallelepiped with sharp edges, comprising an internal structure of aluminium alloy square tubes that held the external aluminium alloy plates. The dimensions of the parallelepiped were 0.45 m $\times$ 0.8 m $\times$ 1.0 m. The building model was equipped with 150 pressure taps (see Fig. 2.9b), of which 31 lay on the top plate , 21 lay on the side plate and 48 lay on the front plate. The remaining taps were located on the other three faces, which were not considered in the present study. The pressures were acquired by means of three low-range 32-port scanners by Pressure System Inc. embedded inside the building model and 20 Kulites XCS-093 transducers for the unsteady pressure measurements in selected positions (see Figure 2.9b).

Due to the lack of a well-defined dynamic pressure in the wind-off tests, the pressure results will be presented by the pressure coefficient c_P:

$$c_P = \frac{P - P_\infty}{\frac{1}{2}\rho V_{\text{IND}}^2}, \tag{2.1}$$

where P_∞ is the static far-field pressure and V_{IND} is the estimated rotor-induced velocity according to the Momentum Theory (MT) [37] which is defined as:

$$V_{\text{IND}} = V_{\text{TIP}}\sqrt{\frac{c_{T,OGE}}{2}}. \tag{2.2}$$

However in the wind-on test, the standard definition of the pressure coefficient will

also be adopted, identified by the * superscript:

$$c_P^* = \frac{P - P_\infty}{\frac{1}{2}\rho U_\infty^2}. \tag{2.3}$$

The declared accuracy of the pressure scanners led to an uncertainty in pressure coefficients of approximately $\epsilon_{c_P} = \pm$ 0.15, but previous experience and some tests carried out before the experiment led to measured a c_P repeatability of less than 0.1.

The pressure time-histories were acquired by means of the Kulite sensors using a sample-rate of 25000 Hz, corresponding to a sample every $0.6°$ of blade azimuth. The sample time of $5s$ allowed a frequency resolution of 0.2 Hz for the spectra.

The PIV setup is represented in Figure 2.10. The PIV system comprised a Litron NANO-L-200-15 Nd:Yag double-pulse laser with an output energy of 200 mJ and wavelength of 532 nm, and two Imperx ICL-B1921M CCD cameras with a 12-bit, 1952×1112 pixel array. The laser was positioned on the floor so that the laser sheet was aligned with the X-Z plane (see the layout in Fig. 2.10). The camera line of sight was positioned perpendicular to the laser sheet. In order to achieve better resolution of the image pairs, the measurement area comprised two adjacent windows, one on top of the other, that were acquired simultaneously by the two cameras. The synchronisation of the two laser pulses with the image pair exposure was controlled by a six-channel Quantum Composer QC9618 pulse generator. A PIVpart30 particle generator by PIVTEC with Laskin atomizer nozzles was used for the seeding, which consisted of small oil droplets with diameters of 1-2 μm.

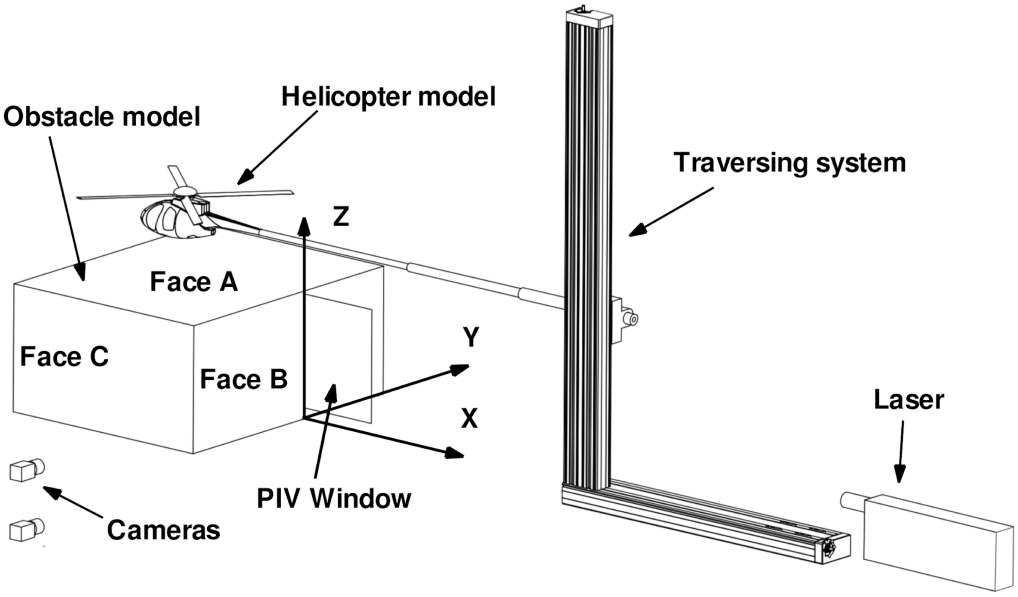

Figure 2.10: *Schematic of the test - PIV setup*

The image pair analysis was carried out using PIVviev 2C software [38], which was developed by PIVTEC in close cooperation with the PIV-Group of DLR. The results that will be shown are the ensemble-averaged measurements over 400 image pairs.

A laser pulse separation time of $\Delta t = 300\ \mu s$ was used and an optical magnification factor of M =4.186 pixel/mm was obtained in the calibration process. Considering the adopted optical magnification factor and the laser pulse delay, the uncertainty of the velocity measurement was estimated to be $\epsilon_u = 0.1/(M\Delta t) = 0.08\ m/s$, since a sub-pixel interpolation algorithm was used.

2.4 Test points - Politecnico di Milano

Tests were carried out with the parallelepiped leaned on the 0.8 m $\times$ 1 m face to represent a low-rise building. With respect to the fixed reference system (X, Y, Z) shown in Fig. 2.11c, several series of tests consisting of vertical sweeps, where X and Y were constant or horizontal sweeps, where Z and Y were constant, were carried out, as represented in Figure 2.11. Table 2.3 lists the parameters used for the different test conditions. The coordinates which identify the helicopter model position refer to the intersection point between the rotor shaft axis and rotor disk.

The various test were carried out both in the wind-off and wind-on configuration. In particular, a wind velocity corresponding to an advance ratio $\mu = U_\infty/(\Omega R) = 0.05$, in order to simulate the effect of a moderate wind that flows past the obstacle. The results of the wind-off test will be presented in section 3.2, whereas the wind-on test will be discussed in section 4.

In order to reduce the balance thermal drifts, each test point corresponded to a single run where the motor was started from rest and then stopped again at the end of the acquisition. The acquisition took place over 5 s long and was preceded by 10 s of flow stabilisation. The balance zeroes were acquired immediately before and after each run and the mean of these two readings was used to account for the balance thermal drift. However, because of the short run time, this zero drift was quite small. The rotational speed was set equal to 2580 rpm (corresponding to M_{TIP} = 0.3), although drifts of up to 30 rpm occurred during the tests. Thus, the actual RPM value was continuously acquired so that the thrust and torque coefficients would be correctly computed. Three runs were carried out for each measurement point, and the obtained results were averaged.

The pressure measurements were contextual to the load measurements, therefore the same experimental procedure was adopted. The PIV measurements were carried out only for the test points of T2 only.

Test name	Obstacle	Sweep direction	X/R	Y/R	Z/R	First point	Last point	$N°$ of points	μ
IGE	NO	Z	0	0	-	$Z/R = 1$	$Z/R = 4$	10	0 / 0.05
T1	YES	Z	-1.07	0	-	$Z/R = 2$	$Z/R = 4$	7	0 / 0.05
T2	YES	X	-	0	2	$X/R = -1$	$X/R = 1$	5	0 / 0.05
T3	YES	Z	2	0	-	$Z/R = 1$	$Z/R = 4.2$	9	0 / 0.05
T4	YES	Z	2	-1.33	-	$Z/R = 1$	$Z/R = 4.2$	9	0 / 0.05

Table 2.3: *Test Points- POLIMI experimental Campaign*

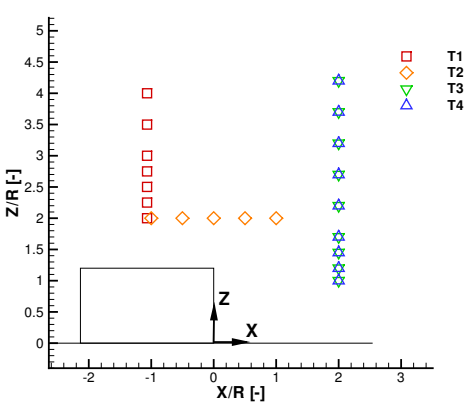

(a) *Test points - Lateral View - POLIMI experimental Campaign*

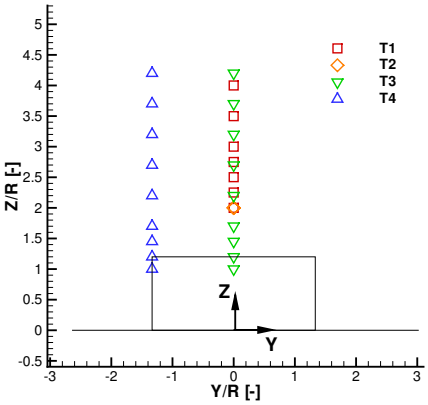

(b) *Test points - Frontal View - POLIMI experimental Campaign*

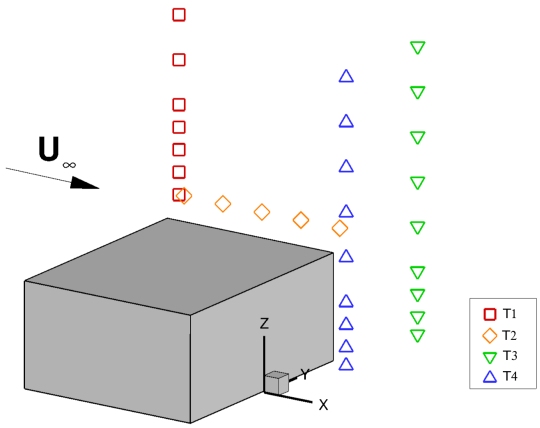

(c) *Test points - 3D View - POLIMI experimental Campaign*

Figure 2.11: *Schematic of the Test Points - Milano experimental Campaign - Each point corresponds to the position of the rotor centre in that test.*

CHAPTER 3

Wind-off Experiments

THE main results of the two experimental campaigns in absence of external wind are presented in this chapter, basically representing different hovering positions of the helicopter model with respect to the obstacle. Firstly the results of the Glasgow experimental campaign are presented in Section 3.1, comprising load and moment measurements on the rotor, LDA measurements of the rotor inflow and Stereo-PIV measurements of the flow-field generated by the interaction. The results of the experimental campaign carried out at Politecnico di Milano are then shown in Section 3.2, comprising load and moment measurements on the rotor, unsteady and averaged pressure measurements on the obstacle and PIV measurements of the flow-field. Eventually,in Section 3.3, a few comparisons are drawn between the results obtained in the two experimental campaigns.

3.1 Experiments results- University of Glasgow

In this section the main results of the Glasgow experimental survey are analysed. The load measurements for the different rotor position are presented in Fig. 3.1,3.2 and Fig. 3.3, the LDA inflow measurements along the x and y rotor-axes are presented in Fig. 3.4 and 3.5. The PIV measurements in the symmetry plane $Y/R = 0$ are presented in Fig. 3.6 (in-plane velocity magnitude contours and streamlines) and 3.7 (out-of-plane velocity contours), while the transverse planes are presented in Fig. 3.8 and 3.9.

A set of load measurements were initially carried out in order to qualify the rotor performance in absence of the obstacle. The rotor was placed as high as possible ($Z/R = 4$) in order to assess the Out-of-Ground-Effect (OGE) condition. A $c_{T,\text{OGE}}$ of $7.36 \cdot 10^{-3}$ and a $c_{Q,\text{OGE}}$ of $8.75 \cdot 10^{-4}$ were obtained, leading to a Figure of Merit of $FM_{\text{OGE}} = 0.51$, as summed up in Table 3.1.

$c_{T,\text{OGE}}$	$7.36 \cdot 10^{-3}$
$c_{Q,\text{OGE}}$	$8.75 \cdot 10^{-4}$
FM_{OGE}	0.51

Table 3.1: *Out-of-Ground-Effect (OGE) reference condition for the Glasgow experimental campaign*

All the results for the thrust coefficient and figure of merit will be presented from now on divided by their respective OGE values, in order to appreciate their variation from the reference condition, while the moment coefficients c_{Mx} and c_{My} will be presented through their ratio with $c_{Q,\text{OGE}}$, so that they are expressed as fraction of the OGE torque. The anglo-italian convention for the thrust and torque coefficients have been used throughout the present work, defined as follows:

$$c_T = \frac{T}{\rho V_{TIP}^2 A}, \quad c_Q = \frac{Q}{\rho V_{TIP}^2 A R}. \tag{3.1}$$

The pitch and roll moment coefficient are defined as the torque one. The rotor efficiency will be assessed through the Figure of Merit, defined as:

$$FM = \frac{\text{Ideal hovering power}}{\text{Actual hovering power}} = \frac{c_T^{3/2}/\sqrt{2}}{c_Q}. \tag{3.2}$$

The Figure of Merit (FM) is the ratio between the ideal rotor power coefficient required in hovering flight, estimated through the Momentum Theory as $c_T^{3/2}/\sqrt{2}$, and the measured power coefficient, which is equal to the torque one.

The results corresponding to the test point where the rotor was placed in the symmetry plane of the problem ($Y/R = 0$) will be first addressed in Section 3.1.1, then those at $Y/R = 1$ will be commented in Section 3.1.2.

3.1.1 Results, rotor placed in the symmetry plane $Y/R = 0$

Variation of the thrust coefficient with respect to the out-of-ground-effect (OGE) condition is presented in the plots of Fig. 3.1a, 3.1b and 3.3a. The typical thrust increase (up to 20%) due to the ground effect can be appreciated in both the region over the centre of the obstacle and far from the obstacle, since the relative distance to the closest surface (either the floor or the top of the obstacle) is the same ($1R$) and the rotor projection lies completely on the obstacle top face. However two main regions where the rotor performance deviates from the nominal behaviour can be observed.

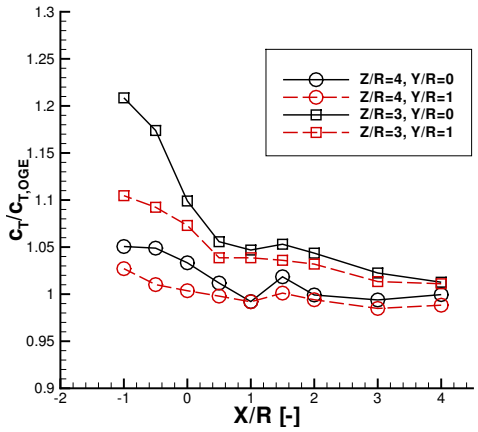

(a) *Ratio between the Thrust Coefficient c_T and the one measured in OGE, $Z/R = 3, 4$*

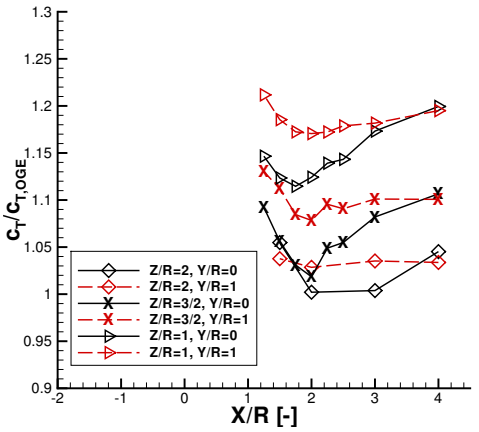

(b) *Ratio between the Thrust Coefficient c_T and the one measured in OGE, $Z/R = 1, 3/2, 2$*

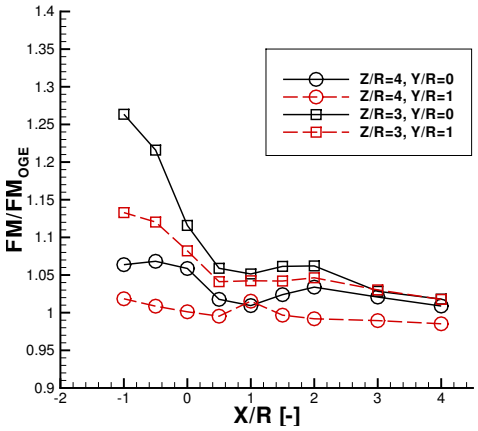

(c) *Ratio between the Figure of Merit and the one measured in OGE, $Z/R = 3, 4$*

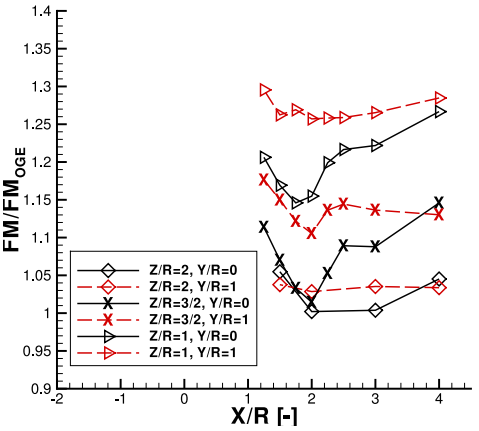

(d) *Ratio between the Figure of Merit and the one measured in OGE, $Z/R = 1, 3/2, 2$*

Figure 3.1: *Thrust coefficient and Figure of Merit vs rotor position, at different rotor heigths*

The first region is the one above the edge of the obstacle, where the thrust coefficient decreases as the rotor is positioned outwards, owing to the minority of the rotor lying over the upper surface of the obstacle. This phenomenon can be appreciated also in the inflow profile of Figure 3.4a measured by means of the LDA system. In this case a gradual reduction of the inflow velocity is observed going from $X/R = 1$ to $X/R = -1$, as prescribed by the ground effect. However, one would expect this variation to be non-symmetrical, since only part of the rotor projection lies on the top of the obstacle and thus is affected by the ground effect. Conversely this appears not to be the case since the inflow profile of Fig. 3.4a is pretty symmetrical. This is also testified by the fact that the the pitch and roll moments of Fig. 3.2a and 3.2c are quite close to zero in the region $-1 < X/R < 1$. An addi-

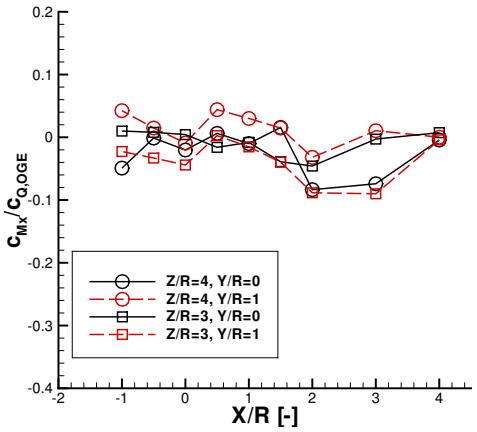

(a) *Ratio between $x-$moment coeff. and the OGE torque coeff., $Z/R = 3, 4$*

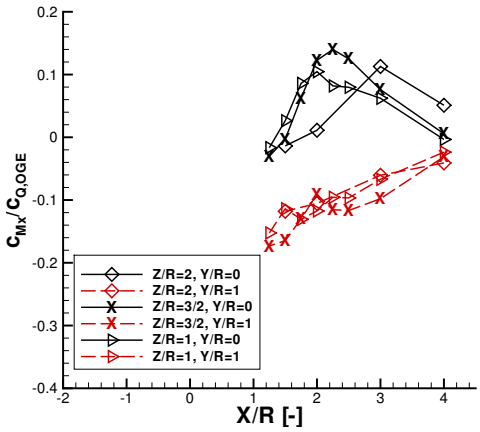

(b) *Ratio between $x-$moment coeff. and the OGE torque coeff., $Z/R = 1, 3/2, 2$*

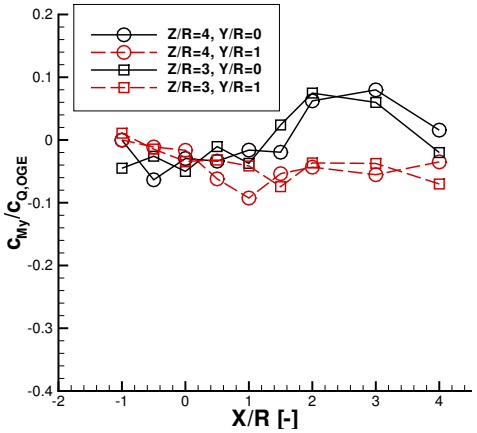

(c) *Ratio between $x-$moment coeff. and the OGE torque coeff., $Z/R = 3, 4$*

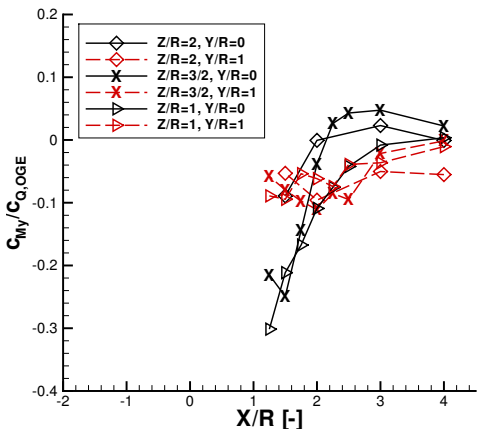

(d) *Ratio between $x-$ moment coeff. and the OGE torque coeff., $Z/R = 1, 3/2, 2$*

Figure 3.2: *x and y moment coefficients vs rotor position, at different rotor heigths*

tional interesting moment behaviour can be observed moving the rotor away from the obstacle ($1 < X/R < 3$) at the same heights ($Z/R = 3, 4$), where a positive $y-$moment develops on the rotor, which fades out in the outer region ($X/R > 4$).

The second region, probably of more interest, is the one just beside the obstacle ($1 < X/R < 3$, $1 < Z/R < 3$), where a severe ground effect reduction can be observed (Figure 3.1b), since the thrust coefficient drops to a value slightly below the OGE one, even at low heights. This behaviour is caused by the development of a recirculation regime in the region between the rotor and the obstacle. The rotor wake, once deflected by the ground, is deflected again by the obstacle and then re-ingested by the rotor itself.

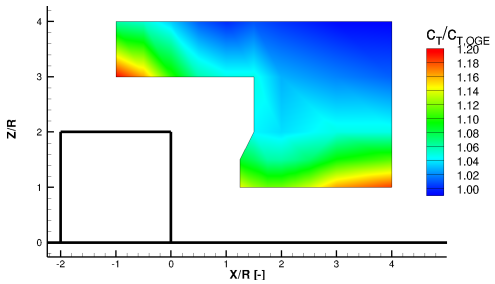

(a) *Ratio between the Thrust Coefficient c_T and the one measured in OGE, $Y/R = 0$*

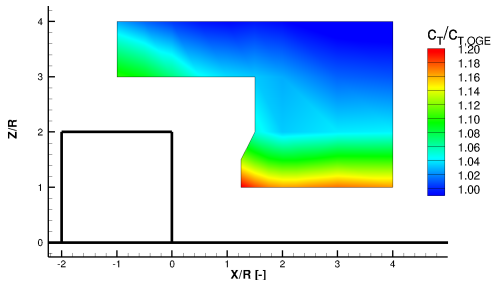

(b) *Ratio between the Thrust Coefficient c_T and the one measured in OGE, $Y/R = 1$*

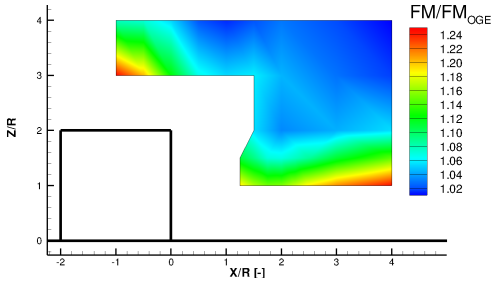

(c) *Ratio between the Figure of Merit and the one measured in OGE, $Y/R = 0$*

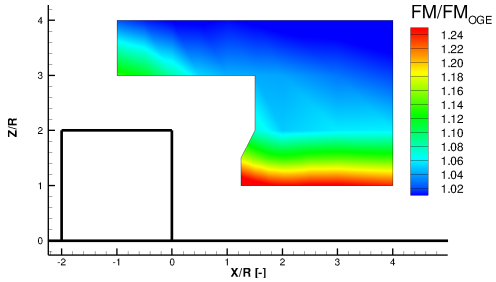

(d) *Ratio between the Figure of Merit and the one measured in OGE, $Y/R = 1$*

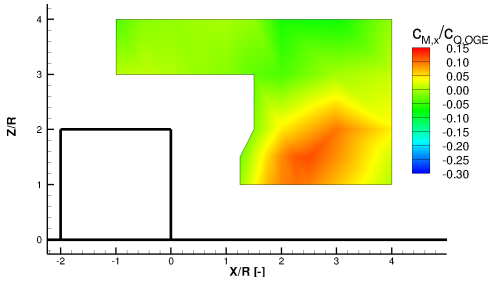

(e) *Ratio between $x-$moment coeff. and the OGE torque coeff., $Y/R = 0$*

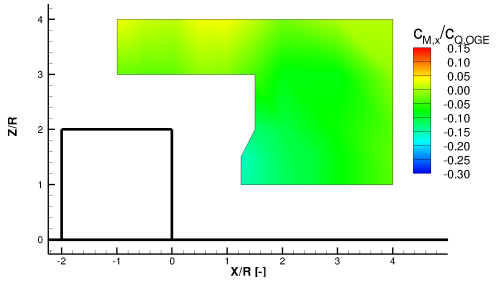

(f) *Ratio between $x-$moment coeff. and the OGE torque coeff., $Y/R = 1$*

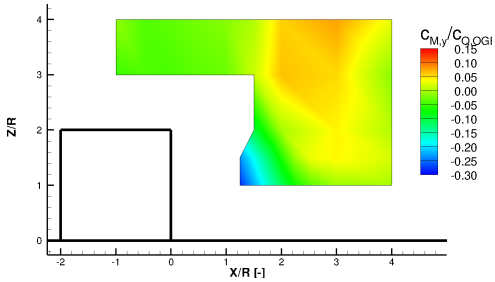

(g) *Ratio between $y-$moment coeff. and the OGE torque coeff., $Y/R = 0$*

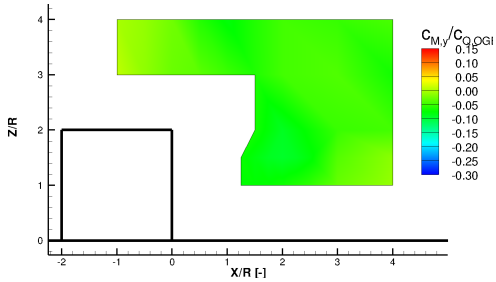

(h) *Ratio between $y-$moment coeff. and the OGE torque coeff., $Y/R = 1$*

Figure 3.3: *Contours of the loads acting on the rotor vs rotor position. Rotor placed at $Y/R = 0$, left, and at $Y/R = 1$, right.*

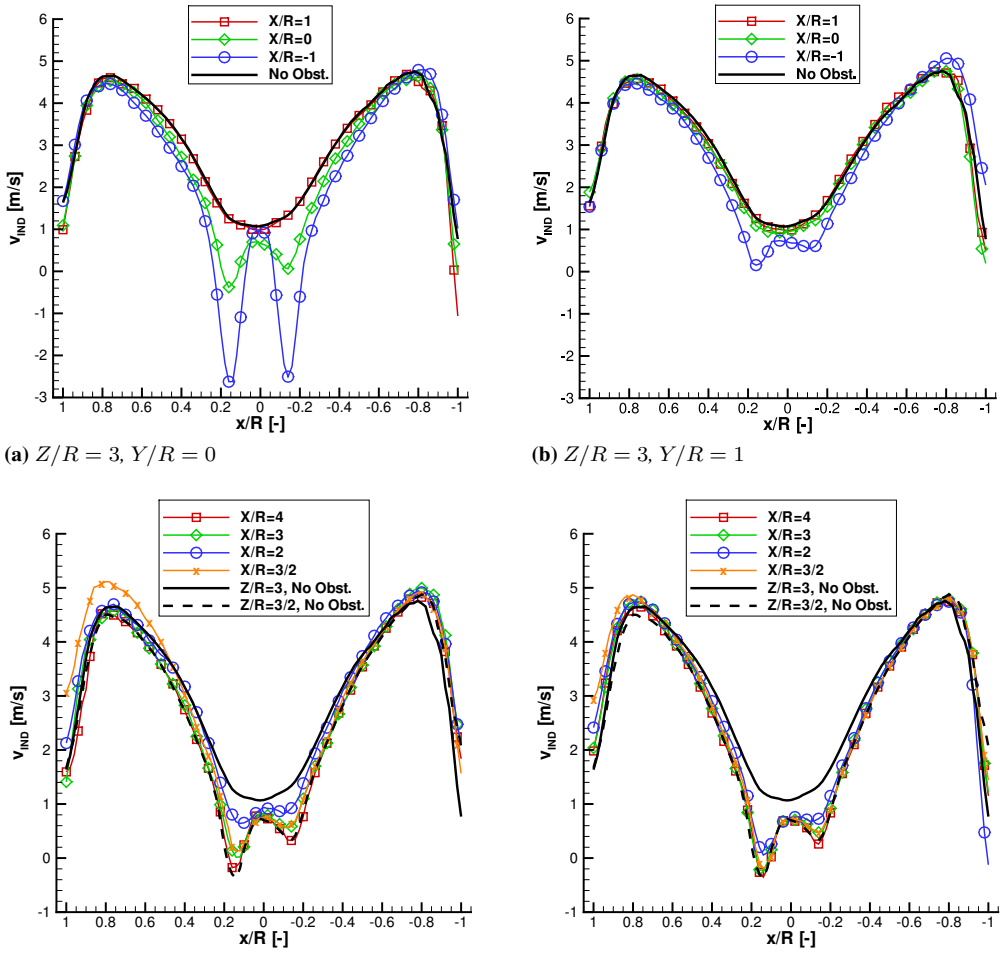

(a) $Z/R = 3$, $Y/R = 0$

(b) $Z/R = 3$, $Y/R = 1$

(c) $Z/R = 3/2$, $Y/R = 0$. *The obstacle is on the left of the plot.*

(d) $Z/R = 3/2$, $Y/R = 1$. *The obstacle is on the left of the plot.*

Figure 3.4: *LDA Measurement of the induced velocity, x-sweep. Rotor placed at $Y/R = 0$, left, and at $Y/R = 1$, right.*

This recirculation region, which is evident in the PIV flow-fields of Figure 3.6, causes an increased induced velocity and a consequent loss of thrust, similar to a partial vortex ring state. This effect is deeply dependent on both the rotor height and distance from the obstacle. A maximum thrust loss of 8% with respect to the furthest rotor position at the same height can be observed at $Z/R = 1$ and $3/2$, whereas at $Z/R = 2$ the maximum thrust loss is lower (approximately 4 $\%$). Moreover one can appreciate the fact that the thrust loss is not monotonic when getting closer to the obstacle, but it presents a local minimum at approximately $X/R = 2$.

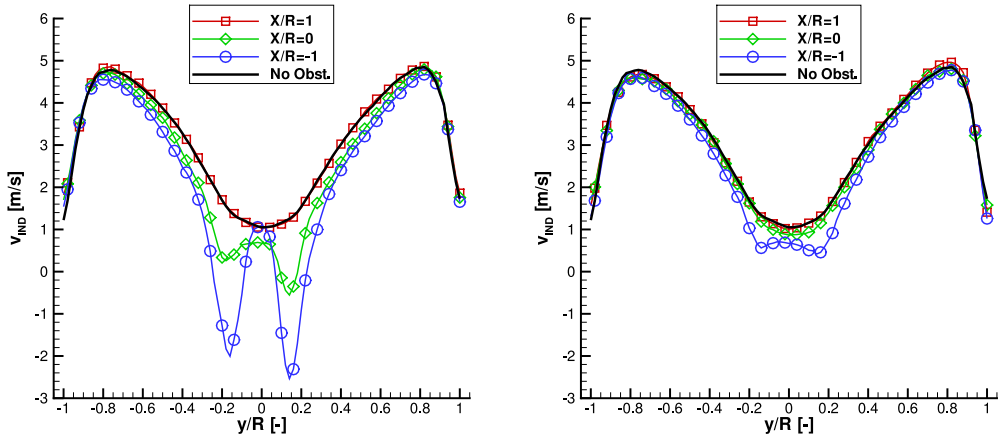

(a) $Z/R = 3$, $Y/R = 0$

(b) $Z/R = 3$, $Y/R = 1$

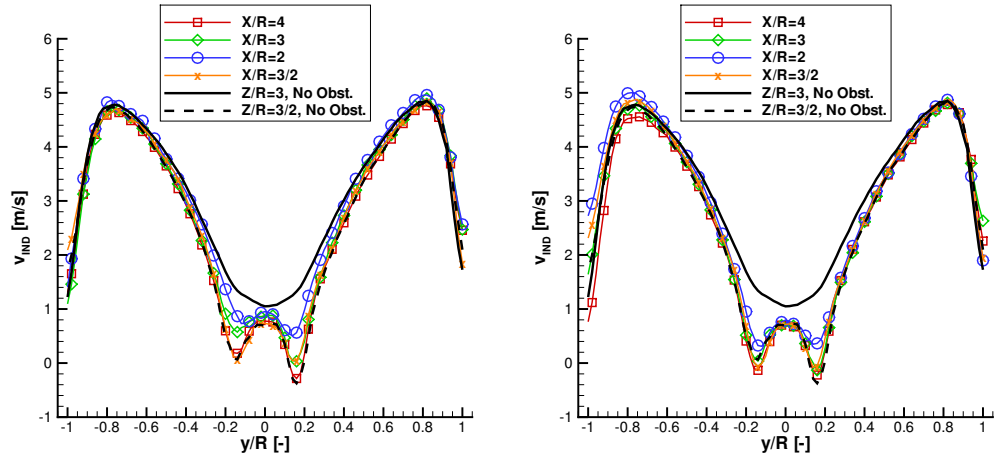

(c) $Z/R = 3/2$, $Y/R = 0$. *The obstacle is on the left of the plot.*

(d) $Z/R = 3/2$, $Y/R = 1$. *The obstacle is on the left of the plot.*

Figure 3.5: *LDA Measurement of the induced velocity, y-sweep. Rotor placed at* $Y/R = 0$*, left, and at* $Y/R = 1$*, right.*

This can be explained looking at Fig. 3.6, where at $X/R = 2$ (Fig.3.6d, 3.6e, 3.6f) the in-plane velocity on the edge of the obstacle (the green layer) is higher than in the other cases (approximately $4\ m/s$ instead of 2.5), thus implying a stronger recirculation. In the other cases (further and closer to the obstacle) most of the air probably flows on the side of the obstacle instead of being redirected upwards. The effect of the obstacle start to be negligible when the rotor is further than 4 radia from the obstacle itself. Another important feature of this region is the arising of a strong pitching moment (up to 30% of the measured torque, Figure 3.3g). This is due to the fact that the previously-introduced recirculation region mainly affects the portion of the rotor closer to the obstacle as it is shown in Figure 3.4c, where an increased induced velocity can be observed in the left portion of the

inflow profile for $X/R = 3/2$. Consequently, a negative c_{My} moment is generated on the rotor, which is evident in Figure 3.2d and 3.3g for $Z/R = 3/2$ and $Z/R = 2$ close to the obstacle, which is equivalent to a pitching nose-down moment if a helicopter was facing the wall. It must be pointed out that, since we are dealing with a fixed rotor without flap and lag hinges, the blade dynamics is more similar to the one of a propeller than to the one of an fully-articulated rotor, implying that the the rotor responds without the typical 90 degrees lag. However a little lag is nevertheless present due to the blade flexibility, thus probably explaining the contextual presence in this region of a $x-$moment in the plots of Figure 3.2b and 3.3e (even if with a much smaller value with respect to the $y-$moment).

For what concerns the rotor efficiency, quite limited variations of the torque coeffiecient were observed among all the rotor positions (less than 4%), leading to a Figure of Merit behaviour (Figures 3.1c and 3.1d and 3.3c) that is very similar to the thrust coefficient one, given the FM definition (Eq. 3.2).

In order to disclose the main features of the flow-field in the symmmetry plane of the problem $Y/R = 0$, the in-plane velocity magnitude contours and streamlines are presented in Figure 3.6. As we can appreciate, the already introduced recirculation region is present in all the cases, even though its morphology is highly case-dependant. At $X/R = 3/2$ (Figures 3.6a, 3.6b, 3.6c) we can appreciate that the rotor slipstream does not impinge on the floor before being deflected towards the obstacle, but impinges directly on the obstacle. This is due to the formation of a counter-rotating (with respect to the main one) recirculation region on the floor. This region is pushed towards the obstacle as the rotor is moved downwards. At $X/R = 2$ (Figures 3.6d, 3.6e, 3.6f), as already highlighted in the previous paragraphs, the rotor wake impinges on the floor before being deflected by the obstacle and re-ingested by the rotor. The air-layer that goes upwards close to the obstacle is thicker and faster than the other cases, probably indicating a stronger interaction with the rotor (confirmed, as previously stated, by the thrust measurements). Eventually at $X/R = 3$ (Figures 3.6g, 3.6h, 3.6i) the flow pattern is very similar to a non-disturbed rotor wake in ground effect, suggesting that the interaction in this case is weaker (as the load measurements also confirm).

The out-of-plane velocity component measurements are presented in Figure 3.7. As a convention, a positive out-of-plane velocity component corresponds to a vector pointing towards the reader. As we can appreciate the rotor slipstream is associated with a negative v, which is coherent with the fact that the left blade is entering the figure. Conversely the interface regions between the rotor slipstream and the recirculation regions on the ground and on the side of the obstacle are generally associated with a bland positive velocity, which means that in this region the air is going towards the reader. No particular variations of the out-of-plane velocity component are presented varying the rotor position.

Two transverse planes at $X/R = 0.1$ (close to the obstacle) and $X/R = 0.466$ (close to the rotor) were also investigated by means of PIV in order to have a deeper

insight of the recirculating flow field, for two different rotor positions: $X/R = 3/2$, $Z/R = 2$ (Figure 3.8) and $X/R = 2$, $Z/R = 2$ (Figure 3.9).

Let us first analyse the plane at $X/R = 0.1$. When the rotor is positioned at $X/R = 3/2$, the rotor wake directly impinges on the lower part of the obstacle, as previously appreciated in flow-field in the symmetry plane of Figure 3.6c. This is also evident in Figure 3.8a, where the upper part of the obstacle is affected by the upwards velocity of the recirculation region, whereas the lower part presents a downwards velocity. This phenomenon is not present anymore when the rotor is placed further from the building as presented in Figure 3.9a, since the rotor wake impinges on the floor before being deflected towards the obstacle. In both cases the out-of plane velocity component is almost null in correspondence of the obstacle due to its blockage effect. Part of the rotor wake is not deflected by the obstacle, but it skims its lateral faces as highlighted by the two regions on the side of the building characterised by a higher out-of-plane velocity.

The second transverse PIV measurement plane at $X/R = 0.466$ directly slices the rotor wake, which can be recognised as the blue high out-of-plane velocity region. However since the position of the measurement plane with respect to the obstacle is the same for the two cases but the rotor position varies, the two slices result to be representative of different regions of the rotor wake. In the first case (rotor at $X/R = 3/2$), the plane is closer to the rotor, therefore the wake is sliced in at a higher position (Figure 3.9a), whereas in the second case (rotor at $X/R = 2$), the wake has already impacted on the floor and it is going towards the obstacle as it can be appreciated in Figure 3.9b.

3.1.2 Results, rotor placed out of the symmetry plane, $Y/R = 1$

The effect of placing the rotor at $Y/R = 1$, out of the symmetry plane of the problem, is analysed in this subsection. As in the previous case, two main regions where the rotor performance deviates from the nominal behaviour can be observed: the region above the edge of the obstacle and the one on the side of the obstacle.

In the first region, a gradual ground effect can be observed as the rotor is moved over the obstacle, similarly to the tests at $Y/R = 0$. However the experienced ground effect is weaker as it can be appreciated in Figure 3.1a and 3.3b, due to the fact that in the innermost postion $X/R = -1$, just half of the rotor projection lies on the upper surface of the obstacle. This is also evident comparing the LDA inflow measurements of Figures 3.4a and 3.4b: the reduction in the induced velocity is less intense when the helicopter is placed at $Y/R = 1$. However, as for $Y/R = 0$, the inflow profiles remain almost symmetrical, leading to very small x and y moments in the region $-1 < X/R < 1$ (Figure 3.2a and 3.2c).

In the second region, the one on the side of the obstacle, the effect of the flow recirculation on the rotor performance becomes less intense with respect to the tests at $Y/R = 1$, according to the fact that only half rotor faces the obstacle. The thrust coefficient reduction is less pronounced as the helicopter is placed closer to the

obstacle, as it can be appreciated in Figure 3.1b. Consequently also the $y-$moment generated in this region is less intense (Figure 3.3h). However, since just the left portion of the rotor (if we consider the helicopter facing the obstacle) is affected by the recirculating flow, a negative $x-$moment is generated on the rotor, as it can be appreciated in Figure 3.2b. If we imagine the helicopter facing the obstacle, this moment corresponds to a roll moment that promotes a thrust rotation to the left.

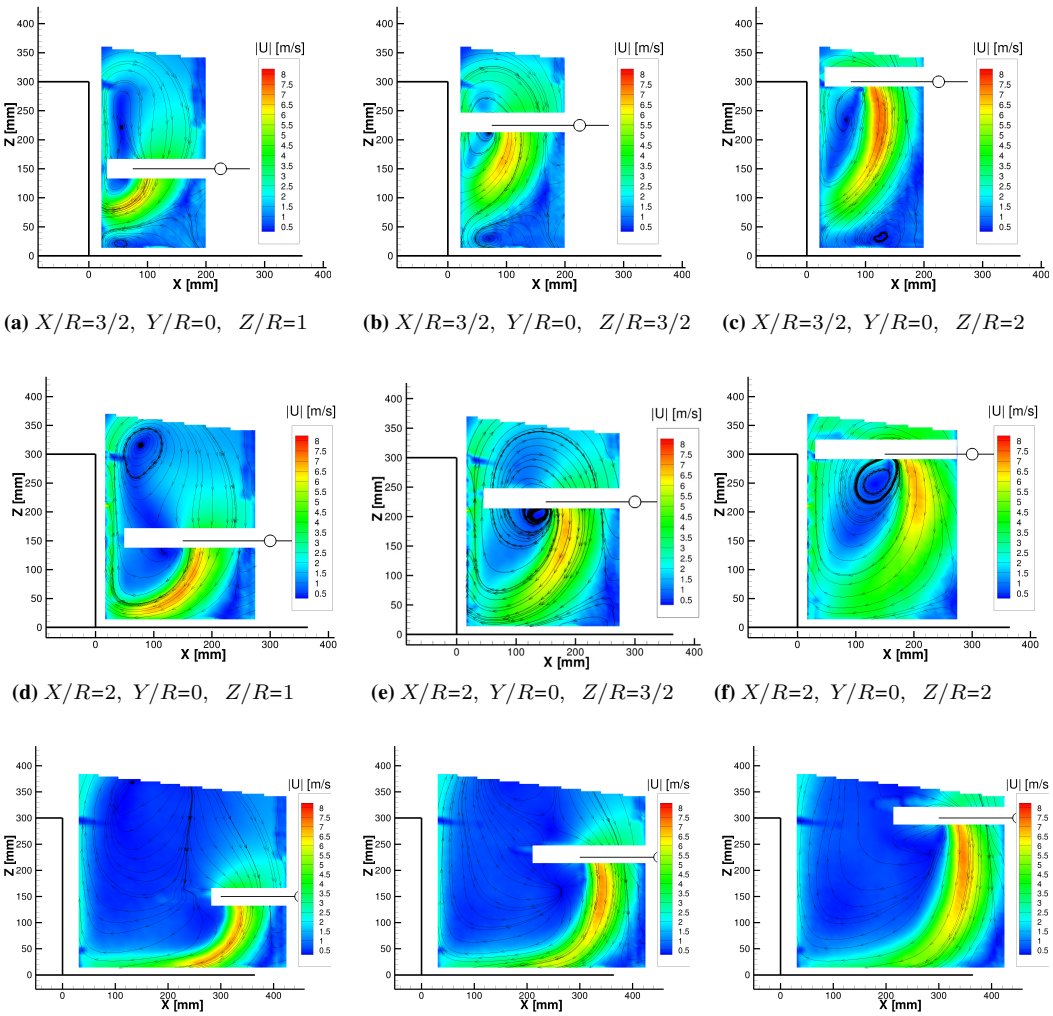

(a) X/R=3/2, Y/R=0, Z/R=1 **(b)** X/R=3/2, Y/R=0, Z/R=3/2 **(c)** X/R=3/2, Y/R=0, Z/R=2

(d) X/R=2, Y/R=0, Z/R=1 **(e)** X/R=2, Y/R=0, Z/R=3/2 **(f)** X/R=2, Y/R=0, Z/R=2

(g) X/R=3, Y/R=0, Z/R=1 **(h)** X/R=3, Y/R=0, Z/R=3/2 **(i)** X/R=3, Y/R=0, Z/R=2

Figure 3.6: *PIV Measurments. In-plane velocity magnitude contours and in-plane streamlines in the problem symmetry plane ($Y/R = 0$) for different rotor positions with respect to the obstacle*

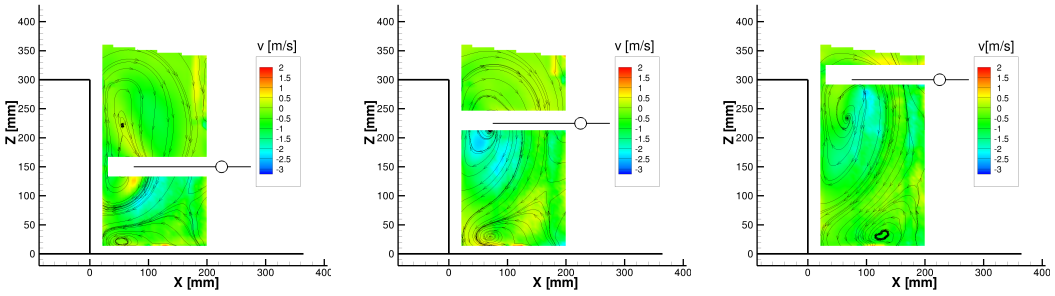

(a) X/R=3/2, Y/R=0, Z/R=1 **(b)** X/R=3/2, Y/R=0, Z/R=3/2 **(c)** X/R=3/2, Y/R=0, Z/R=2

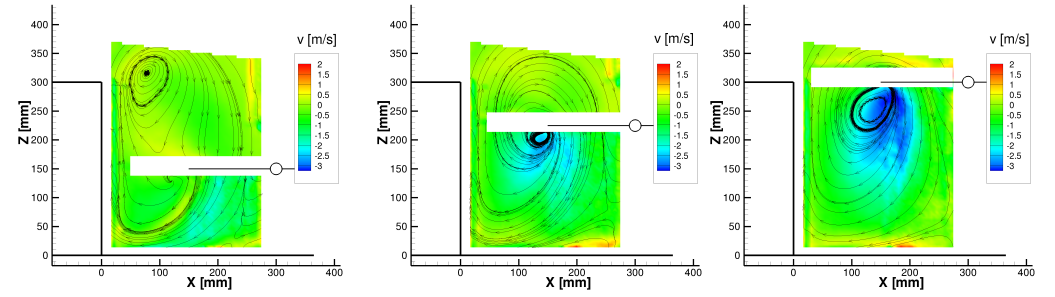

(d) X/R=2, Y/R=0, Z/R=1 **(e)** X/R=2, Y/R=0, Z/R=3/2 **(f)** X/R=2, Y/R=0, Z/R=2

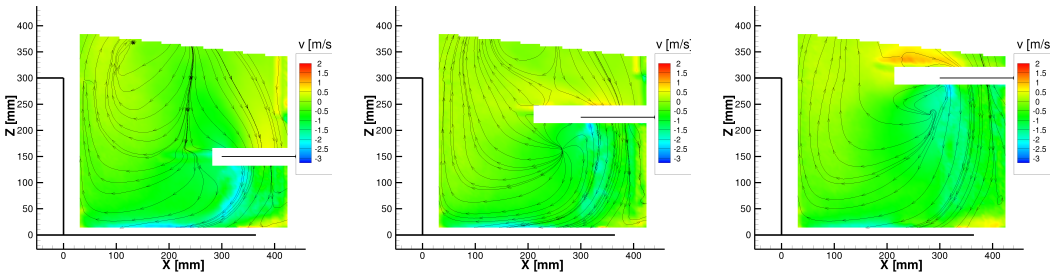

(g) X/R=3, Y/R=0, Z/R=1 **(h)** X/R=3, Y/R=0, Z/R=3/2 **(i)** X/R=3, Y/R=0, Z/R=2

Figure 3.7: *PIV Measurments. Out-of-plane velocity contours and in-plane streamlines in the problem symmetry plane ($Y/R = 0$) for different rotor positions with respect to the obstacle. A positive velocity points towards the reader.*

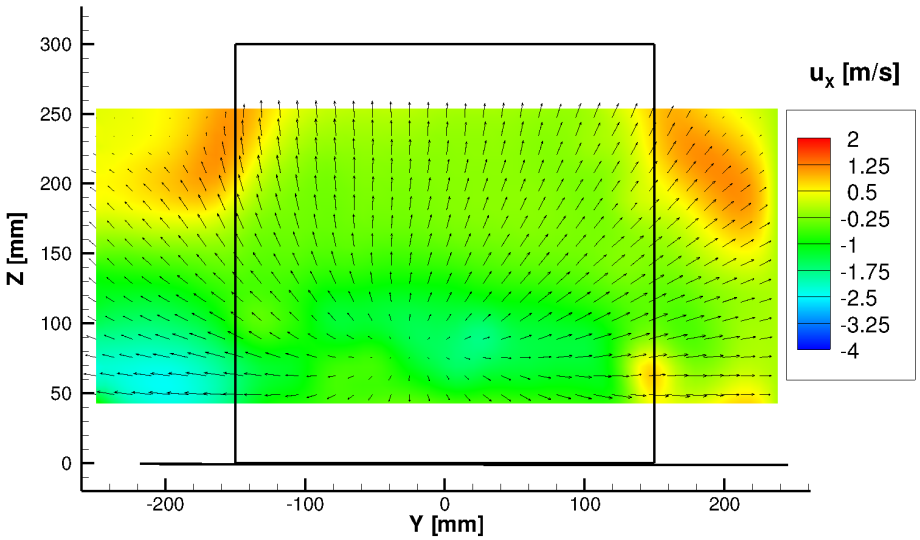

(a) *Transverse measurement plane at* $X/R = 0.1$

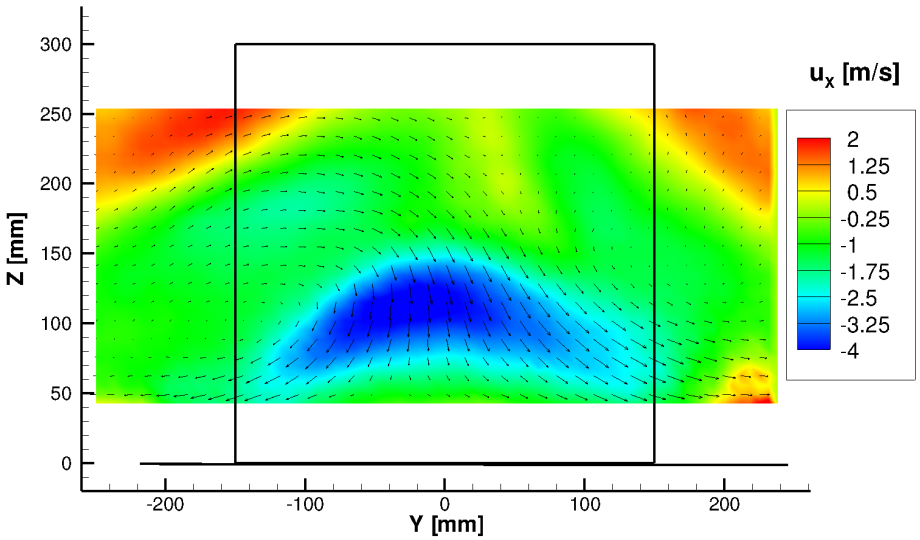

(b) *Transverse measurement plane at* $X/R = 0.466$

Figure 3.8: *Out-of-plane velocity contours and in-plane velocity vectors. Rotor Placed at* $X/R = 3/2$, $Y/R = 0$, $Z/R = 2$. *A negative out-of-plane velocity points towards the obstacle*

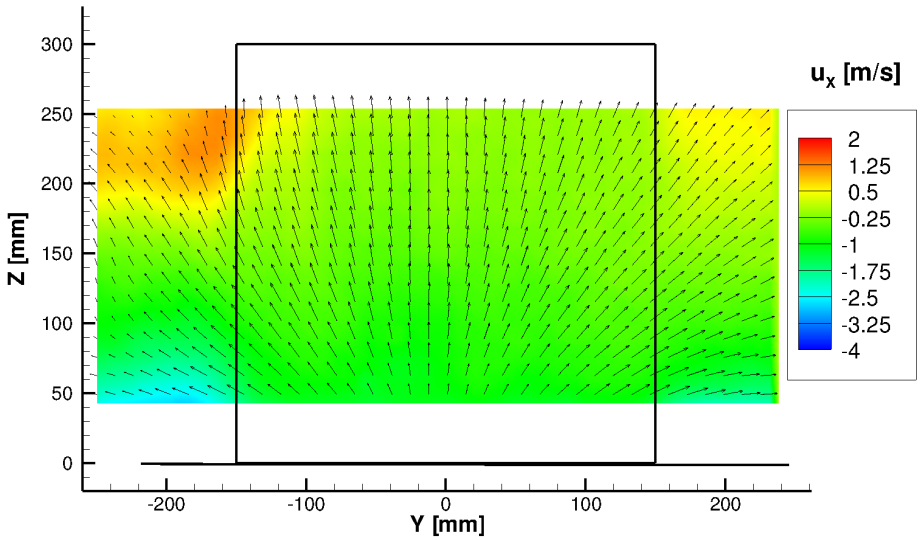

(a) *Transverse measurement plane at* $X/R = 0.1$

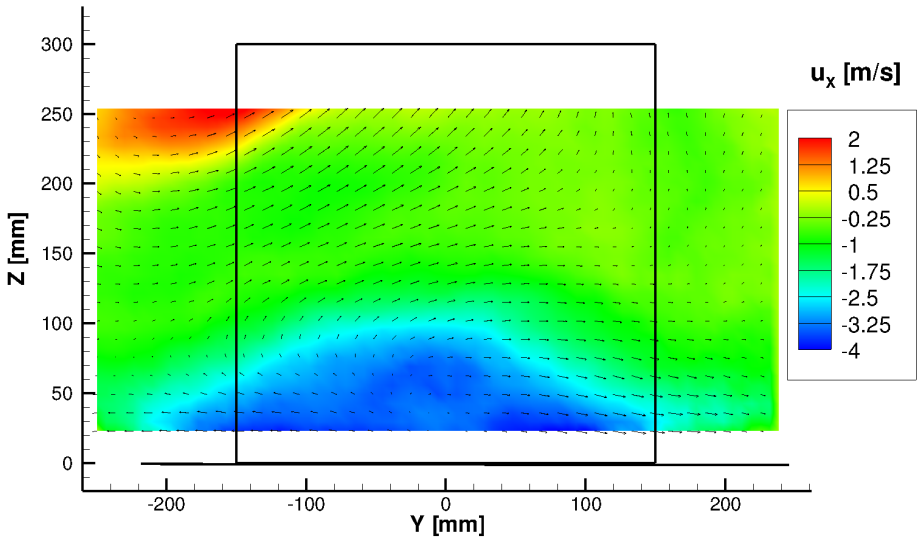

(b) *Transverse measurement plane at* $X/R = 0.466$

Figure 3.9: *Out-of-plane velocity contours and in-plane velocity vectors. Rotor Placed at* $X/R = 2$, $Y/R = 0$, $Z/R = 2$. *A negative out-of-plane velocity points towards the obstacle*

3.2 Experiments results - Politecnico di Milano

The main results of the wind-off experimental survey carried out at Politecnico di Milano are analysed in this section. The thrust and figure of merit measurements for the different tests are presented in Fig.3.11, 3.12 and Fig. 3.13, the averaged pressure measurements on the obstacle are presented in Fig. 3.14, 3.15 and 3.16 and the PIV measurements are presented in Fig.3.17. The results of the unsteady pressure measurements will instead be addressed in chapter 4, together with the results of the wind-on tests.

As in the Glasgow experimental campaign, a set of load measurements were initially carried out in order to qualify the rotor performance in absence of the obstacle. The rotor was placed at $Z/R = 4$ in order to assess the Out-of-Ground-Effect (OGE) condition. A $c_{T,\text{OGE}}$ of $7.27 \cdot 10^{-3}$ and a $c_{Q,\text{OGE}}$ of $7.8 \cdot 10^{-4}$ were obtained, leading to a Figure of Merit of $FM_{\text{OGE}} = 0.561$, as summed up in Table 3.2. The obtained figure of merit is not far from the typical FM for helicopters and is within the expected order of magnitude for a model of this scale without a blade sweep.

$c_{T,\text{OGE}}$	$7.27 \cdot 10^{-3}$
$c_{Q,\text{OGE}}$	$7.8 \cdot 10^{-4}$
FM_{OGE}	0.561

Table 3.2: *Out-of-Ground-Effect (OGE) reference condition for the POLIMI experimental campaign*

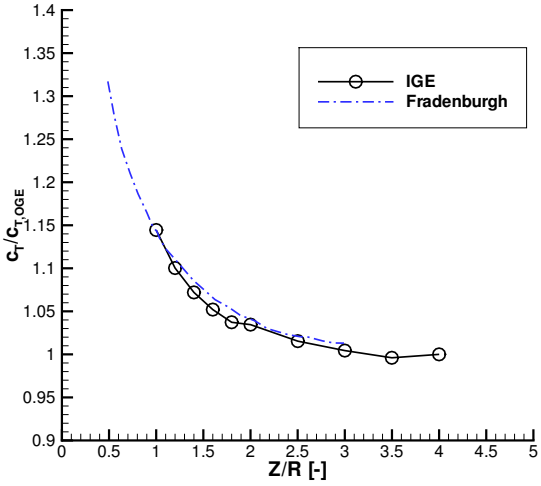

Figure 3.10: *Ground effect test without building model. Results, in terms of the ratio between the thrust coefficient and the OGE one, compared with data from literature (Fradenburgh, [39])*

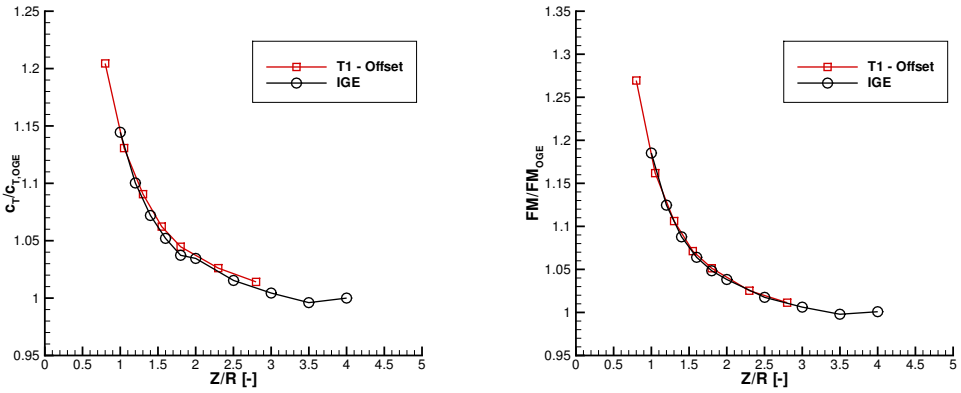

(a) *Ratio between the thrust coefficient c_T and the one measured in OGE*

(b) *Ratio between the figure of merit FM and the one measured in OGE*

Figure 3.11: *Thrust coefficient and figure of merit: Comparison between test T1 and test T2. The curve of test T2 has a Z off-set equal to the building model height ($0.45\ m$ or $1.2R$)*

The first sweep in the Z direction (test IGE of Table 2.3) was carried out without obstacle to produce a reference condition. Figure 3.10 plots the results of this reference test in terms of $c_T/c_{T,OGE}$ and compares them with those obtained by Fradenburgh in [39]. Fradenburgh conducted ground effect tests using a two-bladed rotor, with a diameter of $D = 2ft \simeq 0.6m$ and chord of $c = 2in \simeq 5cm$ operating at V_{TIP} of approximately $600ft/s$, $RPM \simeq 5800$. Despite the difference in geometric and operating conditions, the present results showed good agreement and thus validated the experimental setup.

The first test with the building model (test T1) was a vertical sweep along the vertical projection of the centre of the obstacle upper surface, as an ideal representation of a slow vertical landing on the middle of a flat roof of a low-rise building. In order to more directly compare test T1 with the ground effect of reference test IGE, the results of T1 were plotted with a Z offset equal to the building model height. As shown in Fig. 3.11a, the ground effect experienced above the obstacle is practically equal to the one with an infinite surface underneath, because the whole wake induced by the rotor impinges on the upper surface (see pressure contour in Fig. 3.14a). As in the Glasgow experimental campaign, the torque variations among all the test points were quite limited, leading the figure of merit plots (Fig. 3.13b) to be similar to those of the thrust coefficient. The high-pressure region corresponding to the impingement area of the rotor wake sees a reduced maximum peak as the helicopter is moved away from the obstacle, which implies a reduced ground effect (see Figs. 3.14b and 3.14c). A slight depression was observed on the front face which was washed by the rotor-induced wind.

Test T2 considered a set of points on a horizontal line on the symmetry plane at

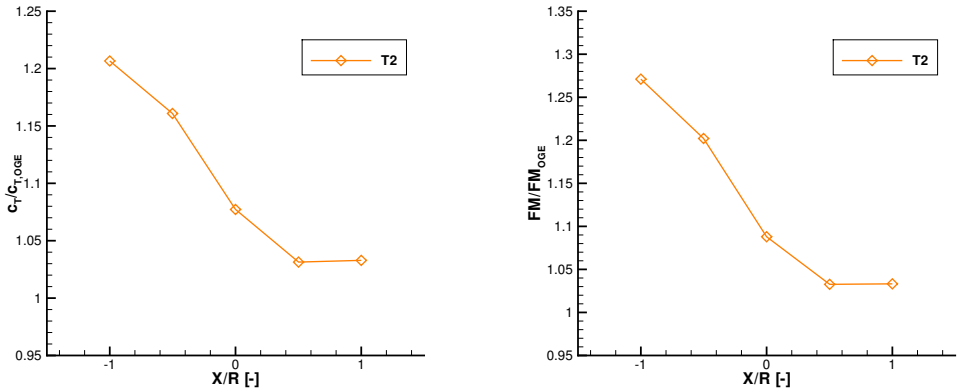

(a) *Ratio between the thrust coefficient c_T and the one measured in OGE*

(b) *Ratio between the figure of merit FM and the one measured in OGE*

Figure 3.12: *Thrust coefficient and figure of merit: test T2.*

$Z/R = 2$. These points can represent a slow horizontal approach to the obstacle upper surface. Figure 3.12a shows the results for X/R varying from -1 to 1. The first considered position is $X/R = -1$; the entire rotor disk is over the obstacle, although not exactly centred with respect to its upper surface (the obstacle centre is at $X/R = -1.07$). For this configuration, $c_T/c_{T_{OGE}} = 1.195$, according to the results of test T1 at the same height. Away from the building centre, the thrust coefficient decreases according to the minor percentage of the rotor projection lying on top of the building. $c_T/c_{T_{OGE}}$ is 1.03 for the outer position, just as it was in test IGE at the same height. Figure 3.15 presents the pressure results. The pressure distribution with the model positioned at $X/R = -1$ was substantially equivalent to the results obtained in test T2 at the same height, even if the X position of the helicopter model was slightly different. When the rotor centre lies exactly on the building edge, $X/R = 0$, the pressure distributions on the different faces of the building indicate the presence of a complex flow structure that was markedly asymmetrical. The diagonal pattern on the front face is probably related to the helicoidal structure of the rotor wake. For $X/R = 1$ the helicopter effect was only apparent on the front face, where the measured overpressure is caused by the rotor wake that, once deflected by the ground, impinges on lower part of the obstacle.

Eventually Test 3 and Test 4 consisted in two Z-sweeps behind the building at $X/R = 2$: the first at $Y/R = 0$, in the problem symmetry plane, the latter at $Y/R = -1.33$, behind the obstacle edge. Figure 3.13a compares the measured thrust coefficients with those of test IGE (without building). A c_T value 3% lower than the one measured in OGE condition is present when the rotor is at the same height as the obstacle model for test T3. This performance drop suggests the presence of an augmented induced velocity associated with a strong recirculation

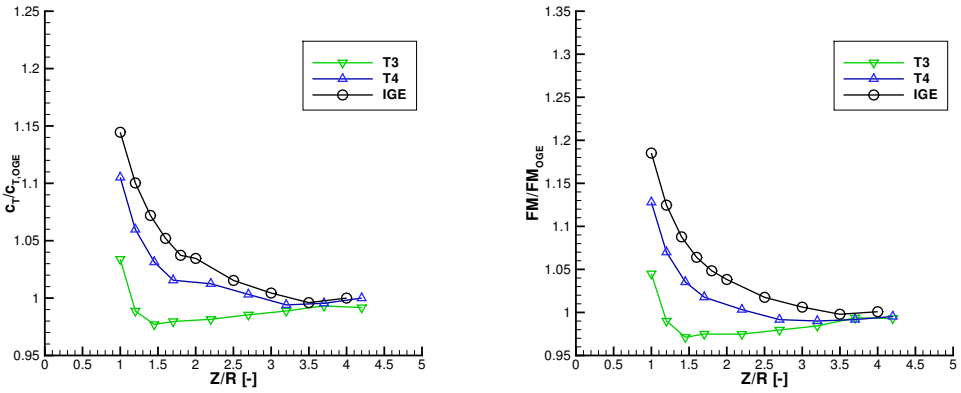

(a) *Ratio between the thrust coefficient c_T and the one measured in OGE*

(b) *Ratio between the figure of merit FM and the one measured in OGE*

Figure 3.13: *Thrust coefficient and figure of merit: Comparison between test T3 and test T4.*

between the building and rotor, as already observed in section 3.1 for the Glasgow experiments. A partial thrust recovery was obtained at lower heights when the helicopter was closer to the ground. The thrust drop becomes negligible from $Z/R = 3$, which is 2.5 times the building height. These detrimental effects appear to be quite mitigated in Test T4, since just half of rotor faces the obstacle, thus leading to a weaker flow recirculation. As observed for the most external point of T2 (Fig. 3.15c), overpressures are apparent on the front face, particularly on the lower part of the obstacle where the wake impinges once deflected by the ground (see Fig. 3.16a). The pressure peak however presents lower pressure coefficient values, due to the increased distance from the obstacle. For test T4, these overpressures obviously interest just the left part of the obstacle. As for test T3, the pressure peak value decreases as the helicopter model is moved upwards. Differently from Test T3, the lateral face of the obstacle is interested by a depression region near the rear edge, which is caused by the left portion of the rotor wake that, once deflected by the ground, skims the considered face.

As highlighted in Test T1, the torque variations among all the tests were generally quite limited, leading the figure of merit plots to be similar to those of the thrust coefficient.

PIV was used to observe the interacting flow field on the building symmetry plane ahead of the building front face (Fig. 2.10). The PIV measurements were carried out for three different longitudinal positions of the helicopter (X/R = -1, 0, 1) at $Z/R = 2$ and $Y/R = 0$, as given in test T2. Figure 3.17 presents the velocity field time-averaged over 400 image pairs. The measured flow fields are visualised by means of the in-plane velocity magnitude contours and in-plane streamlines patterns.

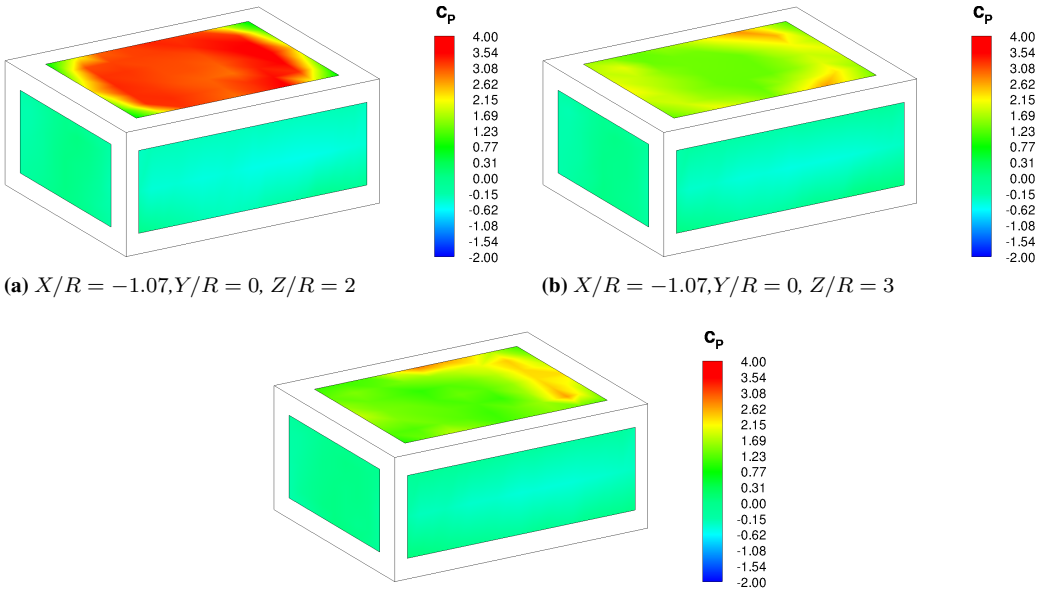

(a) $X/R = -1.07, Y/R = 0,\ Z/R = 2$ **(b)** $X/R = -1.07, Y/R = 0,\ Z/R = 3$

(c) $X/R = -1.07, Y/R = 0,\ Z/R = 4$

Figure 3.14: *Test T1 - Pressure coefficient contours for different helicopter positions.*

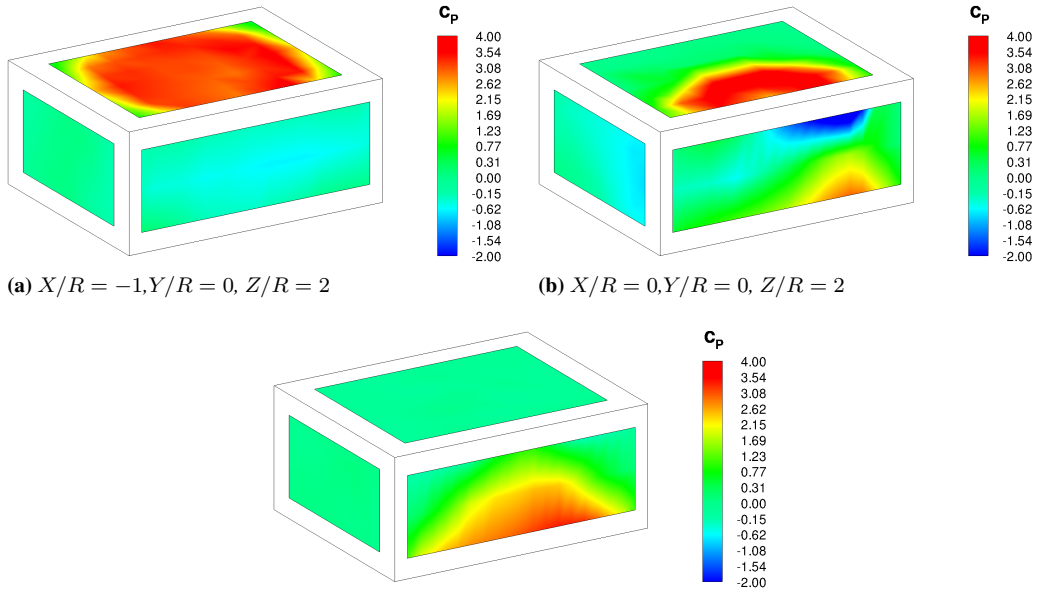

(a) $X/R = -1, Y/R = 0,\ Z/R = 2$ **(b)** $X/R = 0, Y/R = 0,\ Z/R = 2$

(c) $X/R = 1, Y/R = 0,\ Z/R = 2$

Figure 3.15: *Test T2 - Pressure coefficient contours for different helicopter heights.*

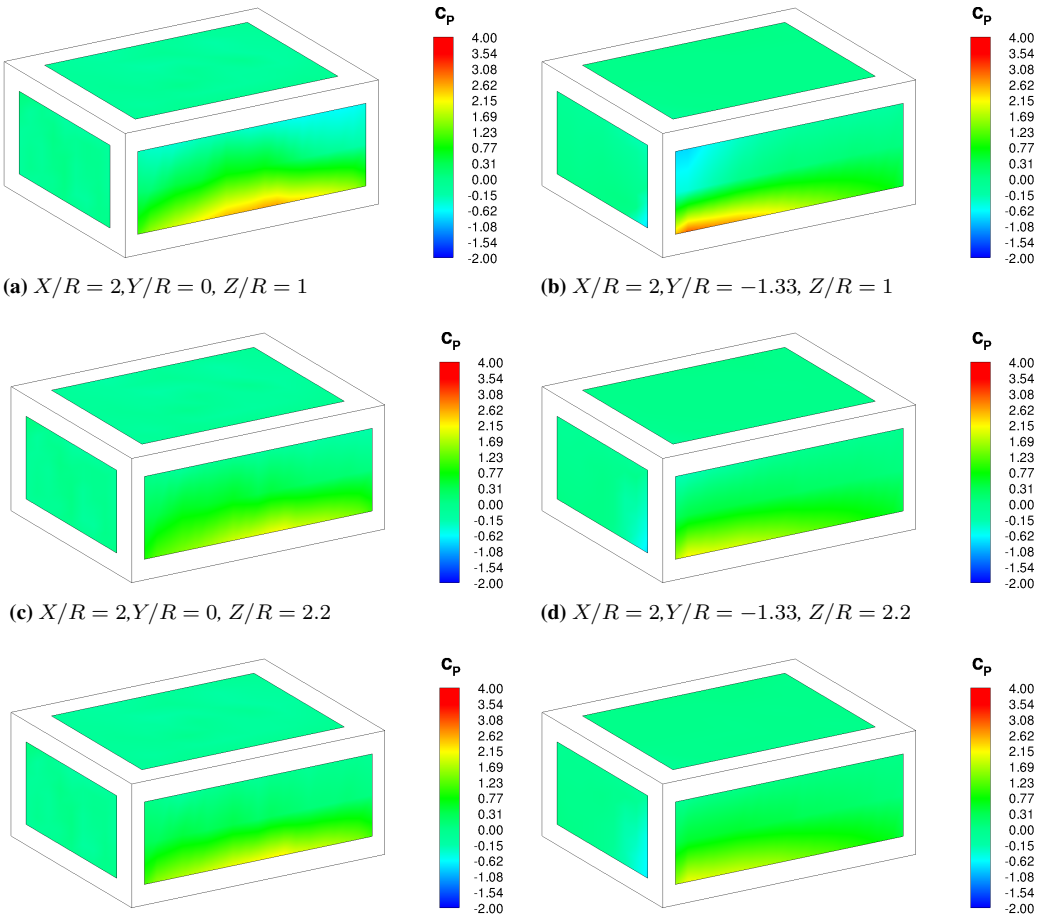

(a) $X/R = 2, Y/R = 0,\ Z/R = 1$

(b) $X/R = 2, Y/R = -1.33,\ Z/R = 1$

(c) $X/R = 2, Y/R = 0,\ Z/R = 2.2$

(d) $X/R = 2, Y/R = -1.33,\ Z/R = 2.2$

(e) $X/R = 2, Y/R = 0,\ Z/R = 3.2$

(f) $X/R = 2, Y/R = -1.33,\ Z/R = 3.2$

Figure 3.16: *Test T3 (left) and Test T4 (right) - Pressure coefficient contours for different helicopter heights.*

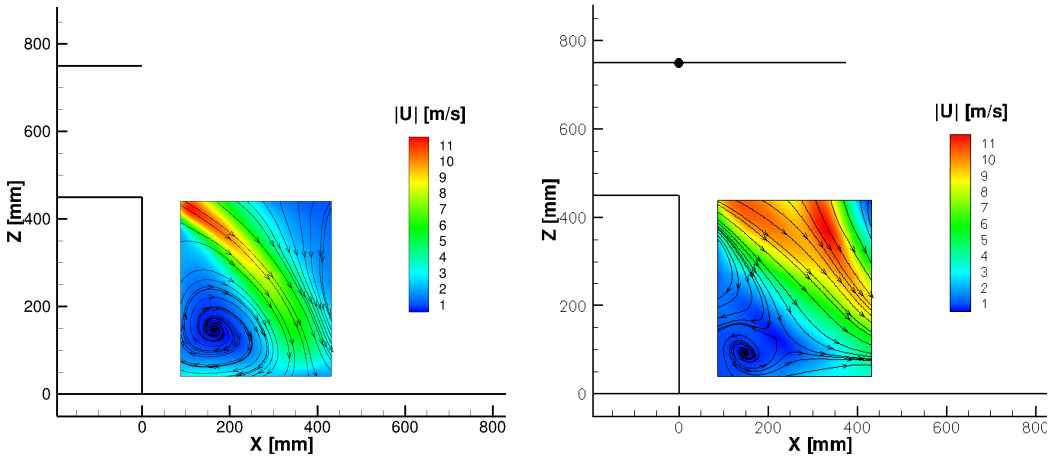

(a) $X/R = -1, Y/R = 0,\ Z/R = 2$ **(b)** $X/R = 0, Y/R = 0,\ Z/R = 2$

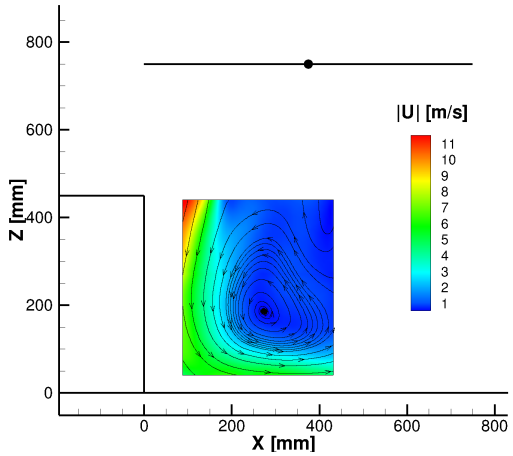

(c) $X/R = 1, Y/R = 0,\ Z/R = 2$

Figure 3.17: *PIV results for test T2: In-plane velocity magnitude contours and streamlines.*

Figure 3.17a clearly shows a high-speed layer issued from the upper face of the obstacle, with the model positioned at $X/R = -1$. This layer originates from the deflection of the rotor wake on the upper surface of the obstacle, inducing a large recirculating region (clockwise in the figure) ahead of the front face. For the test condition at X/R = 0, just half of the rotor wake impinges on the upper surface of the obstacle, as shown by the corresponding pressure pattern of Fig. 3.15b. A clockwise recirculation region produced by the flow blowing from the obstacle was observed also in this case close to the front face, but a series of counter-rotating recirculation regions are also generated in the proximity of the ground . The aft and fore portions of the rotor wake are clearly visible in the upper part of the mea-

surement window. The aft part, once deflected by the upper surface of the obstacle, flows towards the rear part, then merging in a single slipstream.

A completely different behaviour was observed under the last condition (X/R = 1), where the flow topology in the measurement area showed a counterclockwise recirculation region bound by a high-velocity region, corresponding to the rotor fore streamtube boundary (Fig. 3.17c). This high-velocity region is then deflected by the ground away from the obstacle.

3.3 Results Comparison

Even though the test rigs and test conditions adopted in the Glasgow and Milan experimental campaigns were different, several similarities can be found in the results of the two investigations.

Let us start considering the case of a sweep in the X direction over the edge of the obstacle. This corresponds to an horizontal sweep at $Z/R = 3/2$ for the Glasgow experiments, and to the same sweep at $Z/R = 2$ for the Milan experiments (Test T2). Figure 3.18 presents the variation of the thrust coefficient for both experiments in this configuration. $X/R = -1$ corresponds to the rotor being fully over the obstacle, $X/R = 0$ to the rotor centre being over the edge of the obstacle and so on, moving the rotor away from the obstacle for increasing X/R. The results are presented in terms of the ratio with $c_{T,IGE}$, i.e. the thrust coefficient when the rotor is fully in ground effect condition on the obstacle at $X/R = -1$. As we can appreciate, the two experiments highlight the same performance trend which is due to the fact that the ground effect experienced by the rotor is roughly proportional to the percentage of the rotor projection lying on the top of the obstacle, which is the same, at each location, for the two setups. Moreover during this $X-$sweep, very low pitch and roll (close to zero) moments were observed in the Milan experiments (see Fig. 4.9c), exactly as in the Glasgow one. As previously stated in section 3.1, this can be considered a peculiar behaviour, since only part of the rotor projection lies on the top of the obstacle and thus one would expect a non-symmetrical disk loading and a consequent moment. Nevertheless this behaviour was observed in both experiments, thus confirming the effective occurrence of this phenomenon.

Let us now consider the case of a vertical sweep in the Z direction on the side of the obstacle at $X/R = 2$, corresponding to Test T3 of the Milan test matrix. As previously recalled in section 3.1, the region just beside the building is characterised by a recirculation region that causes a loss of thrust and a conspicuous pitch moment on the rotor due to the increased induced velocity on just the part of the rotor which faces the obstacle. Fig. 3.19 presents the comparison between the $y-$moment coefficient (divided by the OGE torque) of the two experiments for the vertical sweep. As it can be appreciated, both experiments show the exact same behaviour, even if with different moment values that probably depend on the differences in the two considered geometries.

When Z/R is less than the obstacle height a negative $y-$moment is apparent,

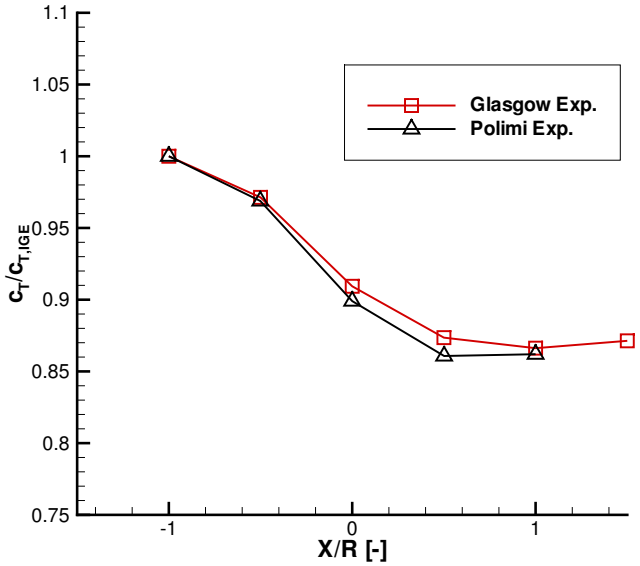

Figure 3.18: *Thrust coefficient as function of the rotor distance from the obstacle edge during an horizontal sweep over the obstacle. Comparison between POLIMI and Glasgow experiments.*

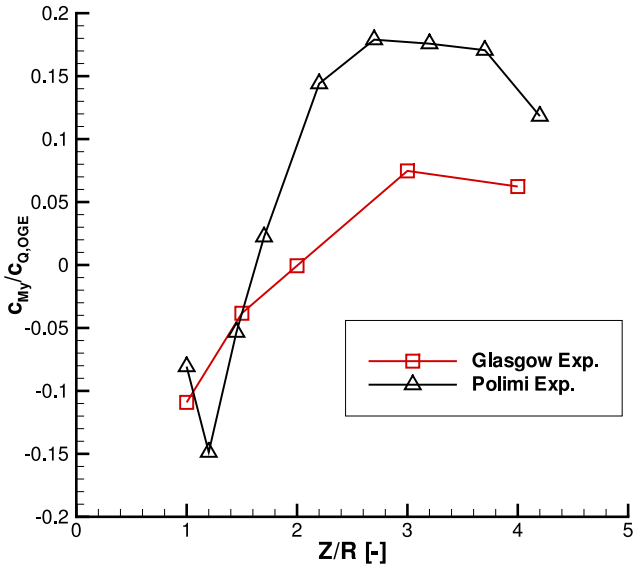

Figure 3.19: *$y-$moment coefficient as function of the rotor height during a vertical sweep beside the obstacle, at $X/R = 2$. Comparison between POLIMI and Glasgow experiments.*

which is equivalent to a pitching nose-down moment if the helicopter was facing the wall, which is consistent with the presence of the recirculation region. As the helicopter is moved upwards, the pitching moment becomes positive, as both experiments testify. The difference in the pitching moment values between the two test test campaign is probably due to the different obstacle height, since this parameter is important for the characterisation of the recirculation region. These discrepancies were not present in the thrust measurements of the horizontal approach (Figure 3.18), because for that test the most important parameter was the percentage of the rotor projection lying on the top of the obstacle, which is the same, at each location, for the two setups.

In conclusion, despite the differences in the test rigs and test conditions adopted in the Glasgow and Milan experimental campaigns, very comparable results were obtained in terms of rotor performance, thus giving a rather strong trust in the fact that the highlighted phenomena are indeed quite general and not typical of just one configuration.

CHAPTER 4

Wind-on experiments

THE main results for the wind-on experimental campaign are presented in this chapter. Firstly a brief description of the flow that develops around a general wall-mounted obstacle is addressed in Section 4.1. Secondly the flow around the specific obstacle geometry in absence of the helicopter is described in section 4.2. Eventually the results for the helicopter-obstacle interaction test in presence of external wind are presented section 4.3 , compared with those obtained for the wind-off case.

4.1 Flow around a wall-mounted obstacle

Before presenting the results of the helicopter/obstacle interaction tests in windy conditions, a brief description of the flow that develops around a wall-mounted obstacle is in order to better understand the morphology of the wake and how it might affect the rotor performance.

This problem has been extensively investigated, by means of both experiments (Martinuzzi and Tropea [40], Liu et al. [41], Sousa [42]) and numerical simulations (Liu et al. [41], Hwang et al. [43], Yakhot et al. [44], Nigro et al. [45]).

The morphology of the flow structures that develop around the wall-mounted obstacle is obviously dependent upon several parameters, such as the obstacle aspect ratio, the thickness of the inflow boundary layer with respect to the obstacle height, the Reynolds number, etc. However, if we just consider low-aspect ratio

obstacles, the main flow structures that occur are mainly originated from the presence of the sharp edges. Thus their morphology may change as function of the flow parameters, but the essence of the occurring phenomena is well-defined. Figure 4.1 shows a schematic of the typical average flow around a low-aspect ratio, wall-mounted obstacle, adapted from Martinuzzi and Tropea, [40]. The flow separation originates in the region upstream of the building, usually at a distance from the obstacle approximately equal to the obstacle height. In particular, the following flow structures develop around the obstacle, if the aspect ratio (width vs height) of the obstacle is sufficiently small:

- A horseshoe vortex that forms at the junction between the obstacle and ground plane upstream of the obstacle, with legs that wrap around the obstacle and become primarily streamwise in the wake. For three-dimensional flows, there is typically an additional thin separation region in front of the horseshoe vortex adjacent to the wall where strong, adverse pressure gradients dominate.

- A series of vortical structures very close to lateral and top surfaces, due to the separation near the leading edges of the obstacle.

- An arch vortex just downstream of the obstacle, consisting of the mean spanwise vortexes shed from the obstacle sides, connected near the upper surface end. This arch vortex entrains the surrounding fluid towards the symmetry plane of the problem.

The separation region behind the obstacle shrinks until it gets to the rear reattachment point, where it gets wider again due to the increase of the mass flux close to the ground as the shear layer reattaches and is subsequently entrained by the horseshoe vortex.

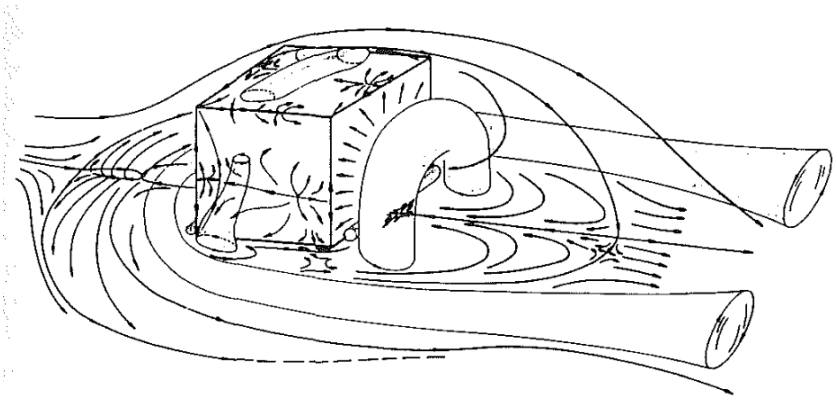

Figure 4.1: *Schematic of the average flow around a wall-mounted obstacle. Adapted from Martinuzzi and Tropea, [40]*

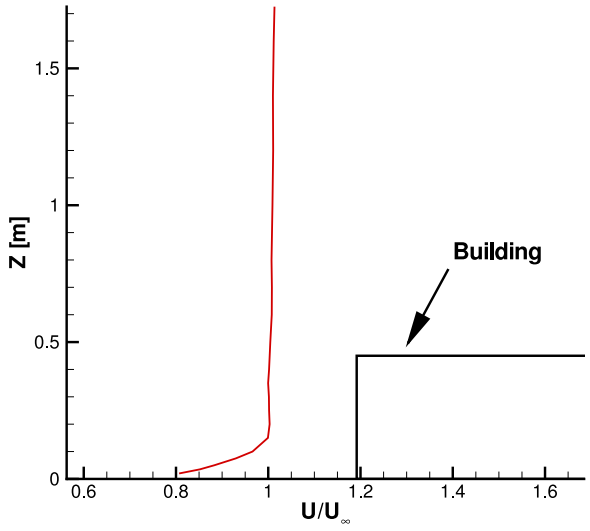

Figure 4.2: *Inflow velocity profile measured at the test section - obstacle sketched for reference*

4.2 Flow around the obstacle without helicopter – Results

As previously stated in section 2.3, all the test in windy conditions were carried out in the large test section of wind tunnel of Politecnico di Milano, which is 14 m wide, 3.84 m high and 38 m long. This test chamber is equipped with several devices allowing to produce different velocity profiles as well as different turbulence intensity and distribution. For the present activity, as no specific real conditions of a specific real site were considered, it was decided to keep the clean flow of the empty chamber, without any upstream turbolator. This flow is characterised by a floor boundary layer thickness of 0.18 cm (40% of the obstacle height) and a mean turbulence level in the order of 2%. The inflow velocity profile, measured at the midspan of the wind tunnel test section in absence of the obstacle, is shown in Figure 4.2. For further information about the features of the flow inside the test section, refer to [46].

A preliminary test was carried out without the helicopter model, in order to obtain the reference condition for the obstacle in windy conditions. The considered wind velocity was U_∞=5.06 m/s, corresponding to an advance ratio of $\mu = 0.05$ if the helicopter was present. PIV measurement of the flow in the symmetry plane downstream of the obstacle is presented in Figure 4.3 by means of the in-plane velocity magnitude contours and streamlines. The arch vortex that develops behind the obstacle is clearly recognisable in the upper-right part of the measurements window, entraining air in the inner part of the obstacle wake.

The pressure coefficient contours are shown in Figure 4.4. The results are presented both in terms of c_P^* (Figure 4.4a) and c_P (Figure 4.4b). As a reminder, c_P^*

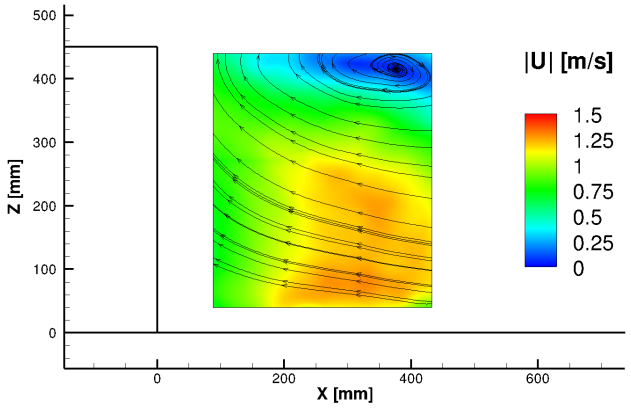

Figure 4.3: *PIV results for $\mu = 0.05$ without helicopter. In-plane velocity magnitude contours and streamlines*

is computed according to Eq. 2.3 using the wind velocity, whereas c_P is computed according to Eq. 2.1 using the estimated rotor induced velocity. As it can be appreciated in Figure 4.4a, the three considered obstacle faces are characterised by a pressure lower than the asymptotic one. The pressure coefficient c_P^* starts from a value approximately equal to -0.8 close to the obstacle leading edge, slowly increasing in both the lateral and top faces up to a value of approximately -0.3, close to the rear part of the obstacle. In the obstacle rear face, the pressure coefficient is almost uniform and equal to -0.3. This behaviour for the pressure coefficient is very similar to the one obtained by Liu et al. in [41] for a wall-mounted cube. The same pressure distribution is shown in terms of c_P in Figure 4.4b, showing lower values with respect to c_P^*. This is due to the different scaling for the pressure; the estimated rotor induced velocity, considering a rotor rotational velocity of 2580 RPM, is $V_{IND} = \Omega R\sqrt{c_{T,OGE}/2}$ =6.1 m/s, which is higher than U_∞, thus leading to lower c_P values. The same results are presented in Figure 4.4c, using the same colorbar range that will be adopted from now on, in order to allow a direct comparison with the pressure results in presence of the helicopter.

The pressure coefficient profiles measured by the Kulite transducers are shown in Figure 4.5a, together with their respective standard deviation σ_{c_P}, represented as error bar, in order to have an indication of the pressure unsteadiness. As a reminder, the pressure taps at $Z/R = 0.2$, 0.6 and 1 are on the obstacle vertical face, while those at $Z/R = 1$ are on the upper surface, close to the obstacle edge, as presented in Figure 2.9b. In general, the pressure taps at $Z/R = 1.2$ experience an higher unsteadiness with respect to those on the vertical face of the obstacle, with a standard deviation of the pressure coefficient of the order of 0.2 against 0.1. This is probably due to the fact that the pressure taps at $Z/R = 1.2$ are close to the trailing edge of the obstacle, from which vortexes are shed into the wake. As for the pressure coefficient contours, Figure 4.5b presents the same results of Figure

4.5a, but using the c_P range that will be adopted from now on, in order to allow a direct comparison with the pressure results in presence of the helicopter. One can appreciate that both the average c_P values and their standard deviations are quite small with respect to the scale of the phenomena that will occur in presence of the rotor.

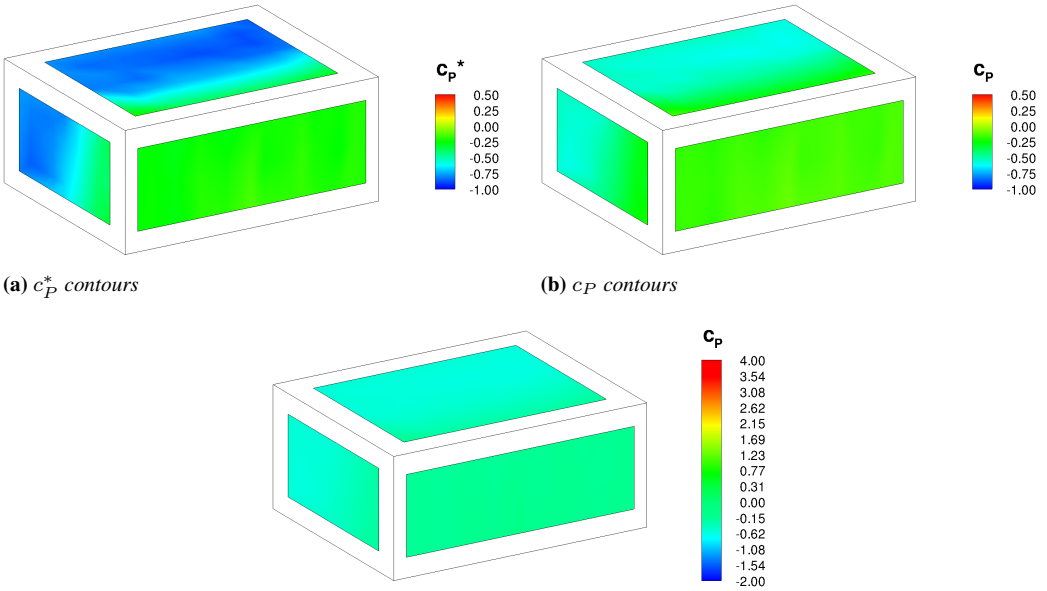

(a) c_P^* *contours*

(b) c_P *contours*

(c) c_P *contours, colorbar values in the range* $[-2, 4]$

Figure 4.4: *Pressure coefficient contours in absence of the helicopter model.* U_∞*=5.06 m/s*

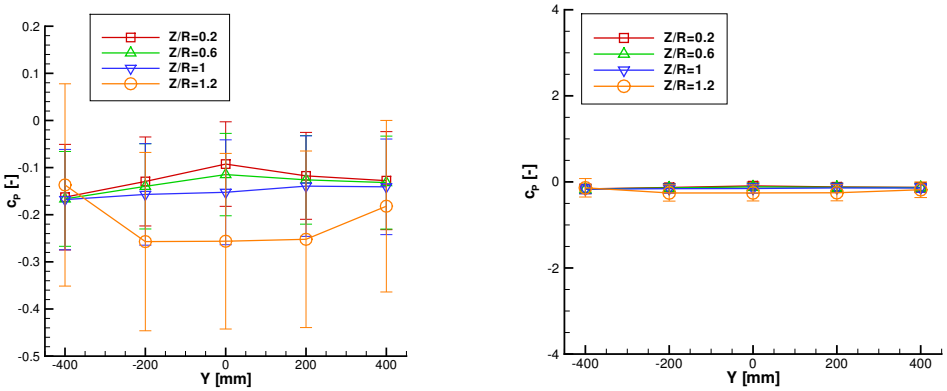

(a) c_P *and* σ_{c_P} *for several pressure taps*

(b) c_P *and* σ_{c_P} *for several pressure taps.* c_P *range* $[-4, 4]$

Figure 4.5: *Averaged pressure coefficient and standard deviation of the pressure coefficient (represented as error bar) in absence of the helicopter model.* U_∞*=5.06 m/s*

4.3 Helicopter-obstacle interaction in windy conditions – Results

The results for the helicopter-obstacle interaction test in presence of external wind ($\mu = 0.05$) are presented in this section, compared with those obtained for the wind-off case ($\mu = 0$). The load measurements are presented in Figures 4.7-4.10; the averaged pressure coefficient on the obstacle is presented in Figures 4.11-4.14, whereas the Kulites measurements are presented in Fig. 4.15-4.17. The pressure fluctuation spectra are presented in Figure 4.18 and eventually the PIV measurements are presented in Fig. 4.19.

Let us firstly consider the test at $Z/R = 4$ in absence of the obstacle, corresponding to the out-of-ground-effect OGE condition. The comparison between the load measurements at $Z/R = 4$ for the wind-on ($\mu = 0.05$) and wind-off ($\mu = 0$) tests is presented in Table 4.1.

	$\mu = 0$	$\mu = 0.05$
c_T	$7.27 \cdot 10^{-3}$	$7.54 \cdot 10^{-3}$
c_Q	$7.8 \cdot 10^{-4}$	$7.63 \cdot 10^{-4}$
FM	0.561	0.606
$c_{Mx}/c_{Q,OGE}$	0.008	-0.14
$c_{My}/c_{Q,OGE}$	- 0,003	1.17

Table 4.1: *Thrust coefficient, torque coefficient, moment coefficients and figure of merit at $Z/R = 4$ without the obstacle: wind-on ($\mu = 0.05$) and wind-off ($\mu = 0$) tests.*

A 4% thrust increase with respect to the wind-off case can be noticed (as already observed by Nacackli and Landman, [17]), which is caused by the combination of the wind speed with the rotational velocity of the advancing and retreating blade. Since the effect on the thrust is quadratic, the thrust increase on the advancing blade is greater with respect to the decrease on the retreating one, thus creating a thrust surplus. A contextual 2% torque contraction is also present, due to the well-known decrease of the induced power in forward flight (see [47]). A small rise in the rotor profile drag is nevertheless presents, but its effect is usually smaller with respect to the decrease in the induced power at this moderate advance ratio. The combination of the thrust increase and the torque decrease leads to a 8% increase for the figure of merit.

The presence of the external wind also produces pitching and roll moments on the rotor. Since a fixed rotor was used for the tests (without swashplate, flap and lag hinges) these moment could not translate in flapping motion, hence the typical 90 degree lag in the blade response was not present.

In particular, a negative roll moment develops on the rotor due to the combination of the wind velocity with the blade rotational velocity. This leads to a higher thrust on the advancing blade and a lower thrust on the retreating one, thus creating a roll moment. A strong nose-up pitching moment, larger than the rotor torque, also develops on the rotor. This is mainly caused by:

- The distribution of induced velocity in forward flight, which is not axisymmetic. In particular, a reduced induced-velocity is experienced in the fore part of the rotor whereas an increased induced-velocity is experienced in the aft part, see [48]. Since no rigid flapping motion is allowed (apart from the one caused by the blade flexibility, which is reasonably small) this induced velocity asymmetry translates in a higher thrust in the fore part of the rotor and a reduced thrust in the aft part, leading to a nose-up pitching motion.
- The effect of the fuselage in advanced flight. As sketched in Figure 4.6, the presence of the fuselage produces an upwash flow in the fore part of the rotor and a downwash flow on the aft part, producing a nose-up moment as in the previous case. However, due to the moderate advance ratio considered, this effect is surely less relevant with respect to the previously described one.

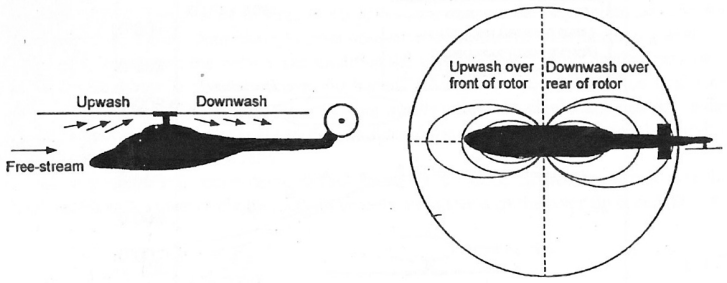

Figure 4.6: *Effect of the fuselage on the rotor inflow in advanced flight. Picture adapted from Leishman, [49]*

Let us now consider the case of test IGE, which comprises tests at several helicopter heights, in absence of the obstacle. As it can be appreciated in Figure 4.7a, the difference in the thrust coefficient between the highest and the lowest helicopter position is smaller in the wind-on case, highlighting a reduced ground effect when the wind is blowing. Moreover the presence of the ground starts to affect the helicopter at $Z/R = 1.5$ in the wind-on case, whereas the ground effect start to be negligible only at $Z/R = 3$ in the wind-off case. To sum up, the ground effect in windy conditions appears to be less intense with respect to the one without wind, and it affects the helicopter only at very low heights. The strong pitch moment gets smaller as the helicopter is positioned downwards, as shown in Figure 4.7c.

As previously described in section 3.2, test T1 represents a ground effect test over the upper surface of the obstacle. As shown in Figure 4.8a, the ground effect experienced over the obstacle is practically equivalent to the one over an infinite surface (Figure 4.7a), exactly as in the corresponding test without wind. In particular in this case the rotor seems not to suffer for the interaction with the obstacle wake above the obstacle. Also the figure of merit (Figure 4.7b) and moment coefficients (Figure 4.7c) show the same behaviour of test IGE. Let us now consider the corresponding pressure coefficient patterns of Figure 4.11. When the rotor is

placed at $Z/R = 2$, as shown in Figure 4.11b, the impingement area of the rotor wake in moved further downstream with respect to the wind-off case, due to the skew angle the wake has in forward flight conditions. A strong depression region develops both on the upper surface of the obstacle, upstream of the high-pressure region, and on the lateral face. When the helicopter is moved upwards, the wake impingement area is moved further downstream, until the obstacle is no more influenced by the rotor for $Z/R = 4$, as shown in Figure 4.11f, which is practically equivalent to Figure 4.4c in absence of the rotor.

Test T2 considered a set of points on a horizontal line on the symmetry plane at $Z/R = 2$. As shown in Figure 4.9a, the gradual ground effects that affected the rotor for $\mu = 0$ as the helicopter is moved on the obstacle, is mitigated in windy conditions. The drop in the thrust coefficient with respect to the wind-off case is up to 7% of the OGE value. Let us now consider the pressure contours of Figure 4.12. Very significant differences in the pressure patterns can be observed between the wind-off and wind-on condition. When the rotor is placed at $X/R = -1$, Figure 4.12b, the high-pressure region corresponding to the wake impingement area is moved downstream, as for test T1. Correspondingly a low-pressure region develop before the impingement area. The pressure fluctuations on the upper surface of the obstacle appear to be slightly mitigated by the wind presence, as it can be appreciated by comparing Figure 4.15a and 4.15b. This can be appreciated also in the pressure spectrum of Figure 4.18a, where the amplitude of the Fourier Transform of the pressure coefficient is presented for the Kulite sensor placed at $X/R = -0.27$, $Y/R = 0.53$, $Z/R = 1.2$, as shown in Figure 4.18d. The considered pressure tap is directly underneath the rotor wake, and the typical $4\times$rev. peak due to one of the four blades passing can be recognised at 172 Hz, as the rotor rotational frequency is 43 Hz.

When the helicopter model is placed at $X/R = 0$, namely directly over the obstacle edge (Figure 4.12d), the pressure pattern on the front face drastically changes with respect to the wind-off case. In particular, the oblique low pressure region is still present, but its peak is less intense and it has moved downwards, approximately at half the height of the obstacle. Consequently the high pressure region on the right of the building looses intensity as well and it is pushed on the left side of the obstacle. The highest time-variability of the pressure coefficient among all test points was measured for this rotor position, both for the wind-off and wind-on case. Let us first consider the test at $\mu = 0$, whose results are shown in Figure 4.15c. All the taps on the front face experience strong pressure unsteadiness, particularly those in the strong depression area ($Z/R = 1$) and in the high-pressure region, where the standard deviation of the pressure coefficient reaches values up to $\sigma_{c_P} = 1$. The pressure taps on the obstacle upper surface ($Z/R = 1.2$), which are washed by the rotor wake, unexpectedly show very limited σ_{c_P}. However this is not verified anymore for the wind-on condition (Figure 4.15d), where also the pressure taps on the obstacle upper surface experience large pressure coefficient

fluctuations over time. This can be also appreciated in the pressure spectrum of Figure 4.18c, where the energy contribution of all frequencies (but especially that of the low-frequencies) is significantly increased for the wind-on case, due to the very unsteady interaction between the rotor and obstacle wakes in this particular configuration. Moreover the 4×rev rotor contribution is mitigated with respect to the test with the rotor placed at $X/R = -1$. Coming back to the standard deviation of the pressure coefficient of Figure 4.15d, the whole front face is still interested by intense pressure fluctuations.

Eventually when the helicopter model is placed at $X/R = 1$, Figure 4.12f, the high-pressure region on the lower part of the front face of the building is drastically reduced, both in terms of extension and pressure peak, with respect to the wind-off case, leaving space to a low-pressure region on its upper part. However, the pressure fluctuations grow drastically in the high pressure region on the lower part of the obstacle ($Z/R = 0.2$), as it can be noticed by comparing Figure 4.15e ($\mu = 0$) and Figure 4.15f ($\mu = 0.05$).

Test T2 was also investigated by means of Particle Image Velocimetry. Figure 4.19 presents the velocity field time-averaged over 400 image pairs. The measured flow fields are visualised by means of the in-plane velocity magnitude contours and in-plane streamlines patterns. For the test condition at $X/R = -1$, the flow morphology of the wind-on configuration (Figure 4.19b) is quite similar to the corresponding wind-off test. However the high-speed layer, originated by the rotor wake deflection, is issued from the upper face of the obstacle with a larger angle with respect to the vertical direction due to the presence of the wind. Greater differences with respect to the wind-off test can be appreciated for $X/R = 0$, Figure 4.19d, and for $X/R = 1$, Figure 4.19f. A reduction of the in-plane velocity magnitude in the rotor wake can be appreciated in both cases, probably indicating that the interaction between the rotor and obstacle wakes produces a remarkable dissipation of the rotor wake energy. For the test point at $X/R = 0$, both the aft and fore portion of the rotor wake are more aligned to the wind direction with respect to the wind-off case, as for $X/R = -1$. Eventually for the test condition at $X/R = 1$ (Figure 4.19f) the fore part of the wake is initially deflected downstream by the wind, but when it reaches the ground it is deflected again in the opposite direction, towards the obstacle, creating an high-pressure region on the lower part of the front face, as already commented for Figure 4.12f. The reduced pressure peak with respect to the wind off case can indeed be explained by the dissipation in the deflected rotor wake that can be observed in Figure 4.19f. Moreover, in this case, the interaction creates a clockwise-rotating flow structure near the obstacle, that was non present for $\mu = 0$, where the rotor wake skimmed the obstacle face.

The load results for Test 3 and 4 are shown in Figure 4.10. As a reminder, Test 3 and Test 4 consisted in two Z-sweeps behind the building at $X/R = 2$: the first at $Y/R = 0$, in the problem symmetry plane, the latter at $Y/R = -1.33$, behind the obstacle edge. Test T3 at $\mu = 0$ was characterised by a severe thrust

drop at low heights due to the development of a recirculation region between the obstacle and the helicopter. This detrimental effect seems to be mitigated in windy conditions (Figure 4.9a), probably due by the fact that the wake of the obstacle does not allow the complete development of such recirculation region. However when the helicopter is completely behind the obstacle, i.e. $Z/R < 1.2$, a slight thrust decrease is nevertheless present. The strong nose-up pitching moment decreases remarkably as the helicopter enters the obstacle wake, as shown in Figure 4.10e, due to the relatively small horizontal velocities with respect to the outer region. A completely different behaviour can be observed for test T4, where the helicopter is placed at different heights behind the obstacle lateral edge $Y/R = -1.33$. A severe thrust coefficient reduction can be appreciated for $Z/R < 1.2$, probably due to the fact that in these test points the rotor interacts with the lateral flow structures of the obstacle wake (i.e. the horseshoe vortex), where strong velocity gradients are indeed present.

Let us now consider the pressure coefficient distribution of Figures 4.13 and 4.14. For test T3 at low rotor heights (Figure 4.13b), the maximum overpressure experienced by the front face of the obstacle is less intense with respect to the same test point at $\mu = 0$, probably due by the weaker recirculation region as also highlighted by the thrust measurements. However the pressure unsteadiness in this region remains substantially high for both cases (Figures 4.16a and 4.16b). The high-pressure region rapidly fades away as the helicopter is moved upwards, due to the skew angle of the rotor wake. For $Z/R = 3.2$ (Figure 4.13f) the pressure pattern is practically equal to the one of Figure 4.4c in absence of the rotor. The behaviour of the pressure coefficient for Test T4, as shown in Figure 4.14, is equivalent at the one of test T3, but it affects mostly the left part the obstacle, due to the different rotor position ($Y/R = -1.33$ for T4 vs $Y/R = 0$ for T3). At the lowest rotor height, $Z/R = 1$ a moderate low-pressure region develops on the upper-right part of the front face, characterised by large pressure fluctuations as shown in Figure 4.17b.

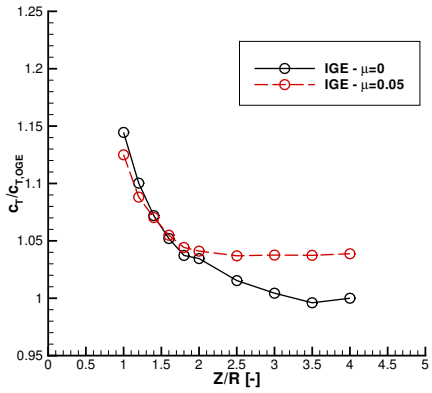

(a) *Ratio between the thrust coefficient c_T and the one measured in OGE*

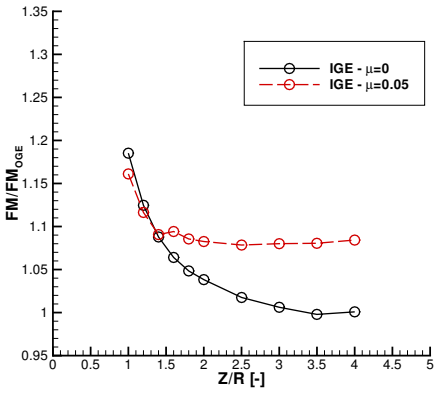

(b) *Ratio between figure of merit FM and the one measured in OGE*

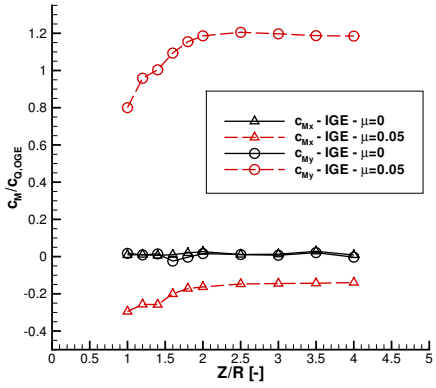

(c) *Ratio between the roll/pitch moment coefficient (c_{Mx} and c_{My} respectively) and the OGE torque coefficient*

Figure 4.7: *Test IGE - Load measurements - comparison between the wind-on ($\mu = 0.05$) and wind-off ($\mu = 0$) tests.*

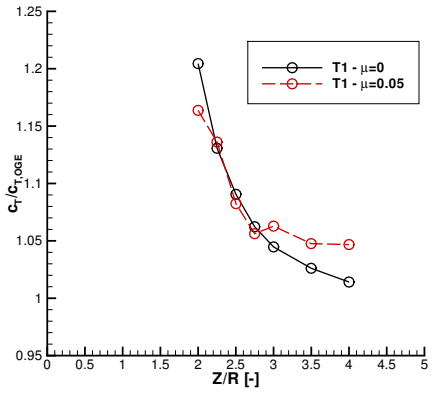

(a) *Ratio between the thrust coefficient c_T and the one measured in OGE*

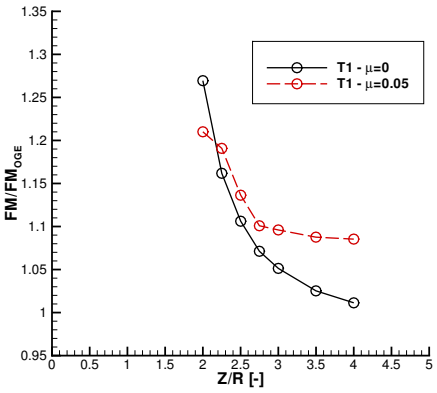

(b) *Ratio between figure of merit FM and the one measured in OGE*

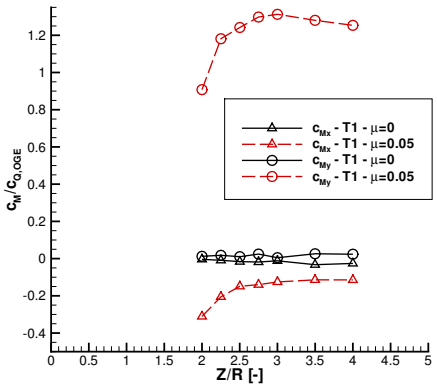

(c) *Ratio between the roll/pitch moment coefficient (c_{Mx} and c_{My} respectively) and the OGE torque coefficient*

Figure 4.8: *Test T1 - Load measurements - comparison between the wind-on ($\mu = 0.05$) and wind-off ($\mu = 0$) tests.*

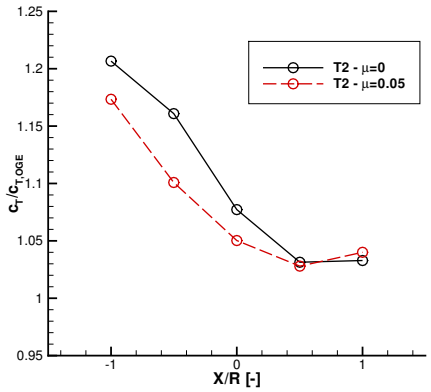

(a) *Ratio between the thrust coefficient c_T and the one measured in OGE*

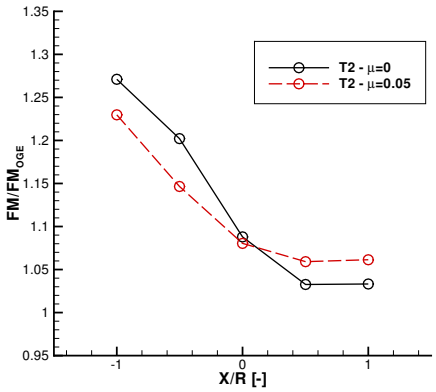

(b) *Ratio between figure of merit FM and the one measured in OGE*

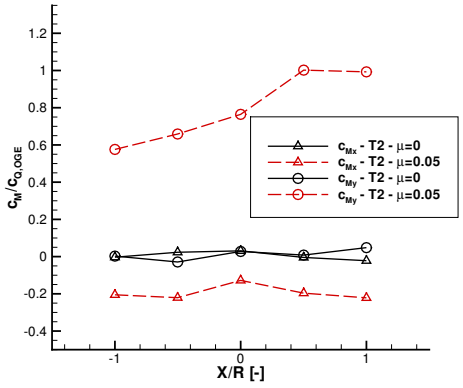

(c) *Ratio between the roll/pitch moment coefficient (c_{Mx} and c_{My} respectively) and the OGE torque coefficient*

Figure 4.9: *Test T2 - Load measurements - comparison between the wind-on ($\mu = 0.05$) and wind-off ($\mu = 0$) tests.*

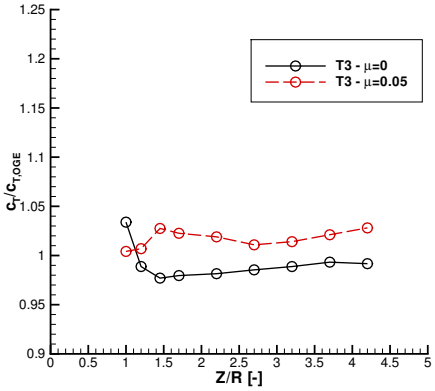

(a) *T3 - Ratio between the thrust coefficient c_T and the one measured in OGE*

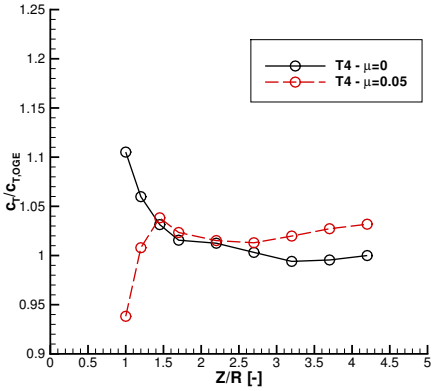

(b) *T4 - Ratio between the thrust coefficient c_T and the one measured in OGE*

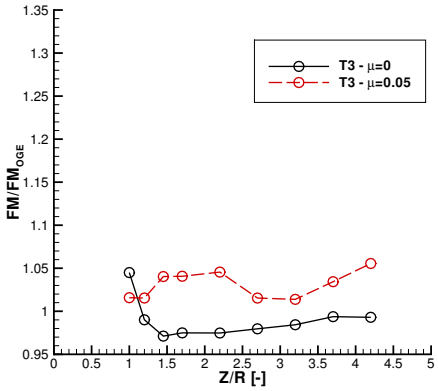

(c) *T3 - Ratio between figure of merit FM and the one measured in OGE*

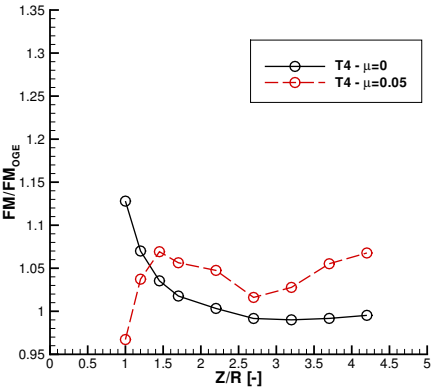

(d) *T4 - Ratio between figure of merit FM and the one measured in OGE*

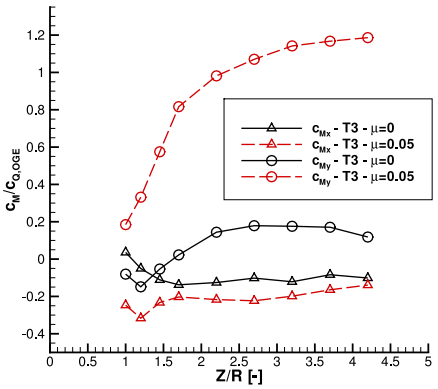

(e) *T3 - Ratio between the roll/pitch moment coefficient (c_{Mx} and c_{My} respectively) and the OGE torque coefficient*

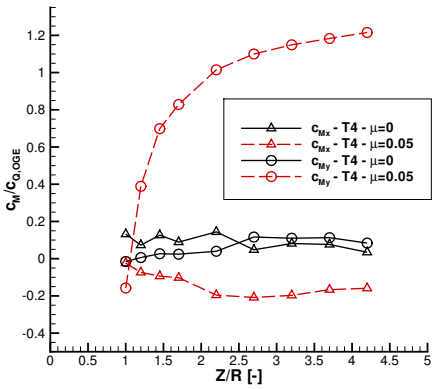

(f) *T4 - Ratio between the roll/pitch moment coefficient (c_{Mx} and c_{My} respectively) and the OGE torque coefficient*

Figure 4.10: *Test T3 (left) and T4 (right) - Load measurements - comparison between the wind-on ($\mu = 0.05$) and wind-off ($\mu = 0$) tests.*

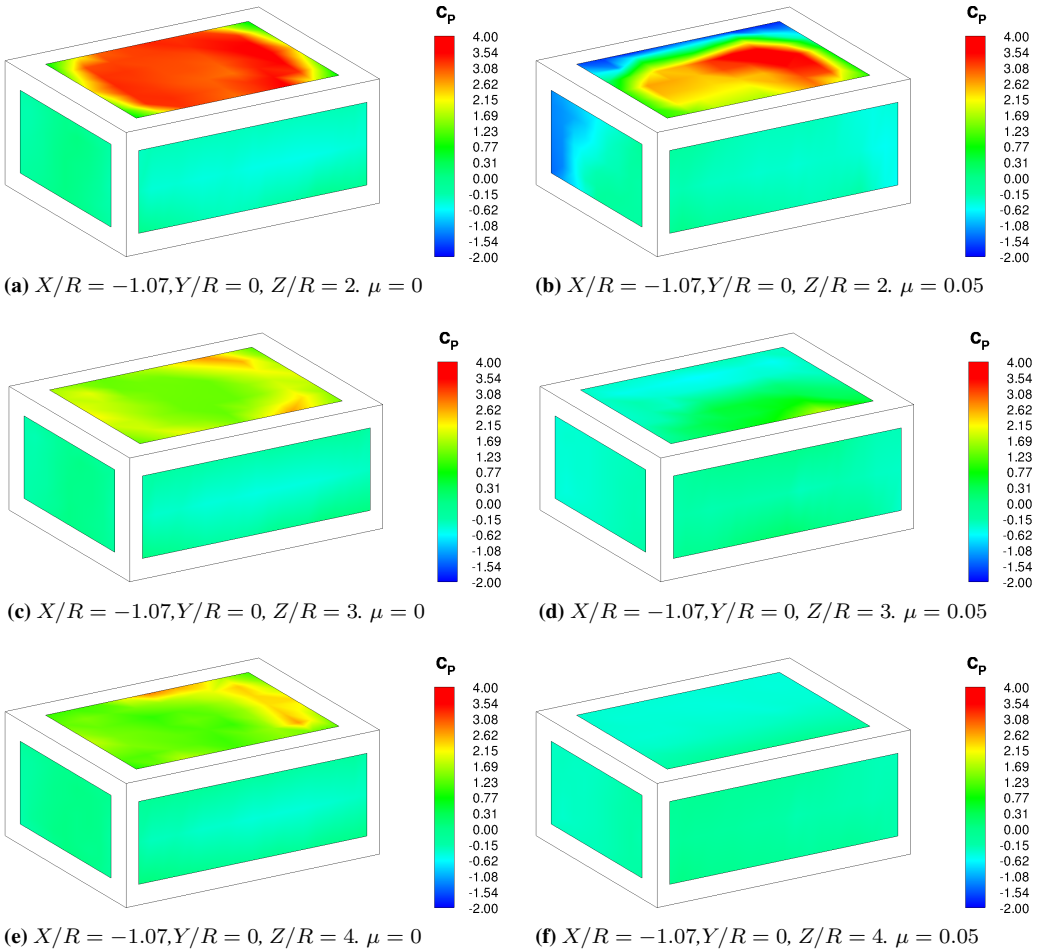

(a) $X/R = -1.07$,$Y/R = 0$, $Z/R = 2$. $\mu = 0$

(b) $X/R = -1.07$,$Y/R = 0$, $Z/R = 2$. $\mu = 0.05$

(c) $X/R = -1.07$,$Y/R = 0$, $Z/R = 3$. $\mu = 0$

(d) $X/R = -1.07$,$Y/R = 0$, $Z/R = 3$. $\mu = 0.05$

(e) $X/R = -1.07$,$Y/R = 0$, $Z/R = 4$. $\mu = 0$

(f) $X/R = -1.07$,$Y/R = 0$, $Z/R = 4$. $\mu = 0.05$

Figure 4.11: *Test T1 - Pressure coefficient contours for different helicopter heights. Comparison between wind-off ($\mu = 0$, left) and wind-on ($\mu = 0.05$, right) tests.*

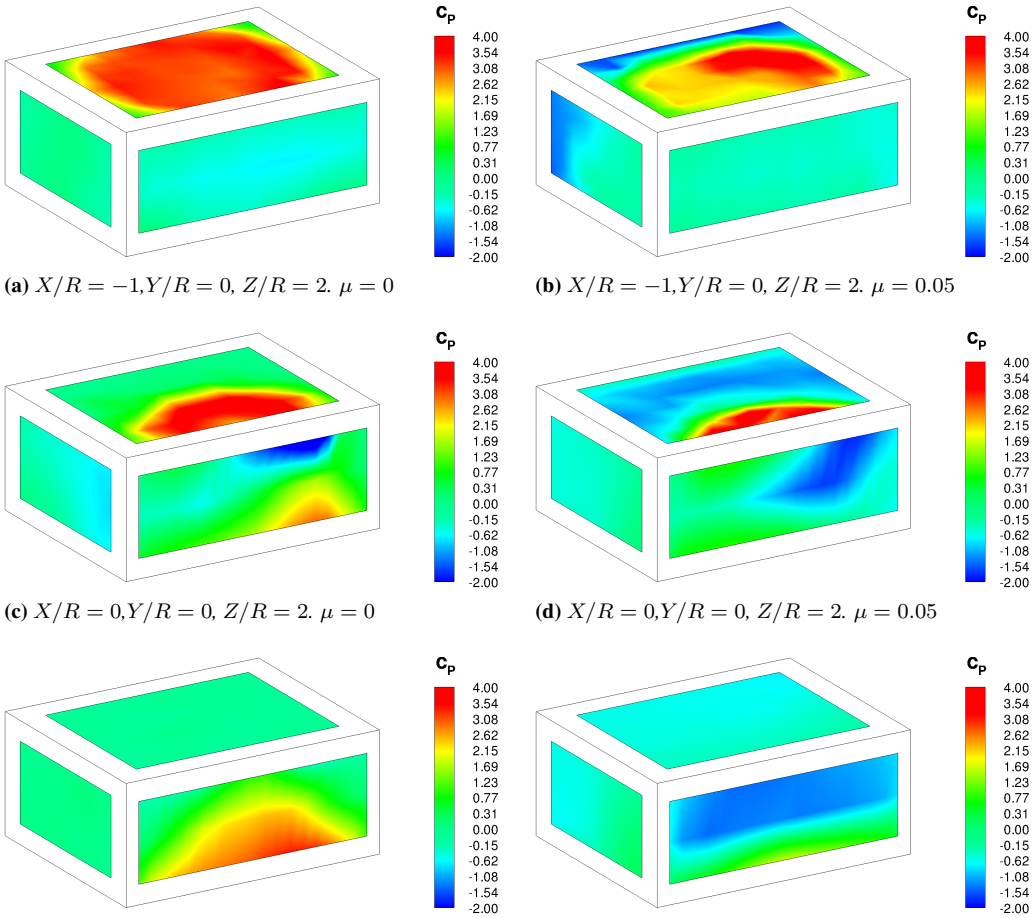

(a) $X/R = -1, Y/R = 0,\ Z/R = 2.\ \mu = 0$

(b) $X/R = -1, Y/R = 0,\ Z/R = 2.\ \mu = 0.05$

(c) $X/R = 0, Y/R = 0,\ Z/R = 2.\ \mu = 0$

(d) $X/R = 0, Y/R = 0,\ Z/R = 2.\ \mu = 0.05$

(e) $X/R = 1, Y/R = 0,\ Z/R = 2.\ \mu = 0$

(f) $X/R = 1, Y/R = 0,\ Z/R = 2.\ \mu = 0.05$

Figure 4.12: *Test T2 - Pressure coefficient contours for different helicopter longitudinal positions. Comparison between wind-off ($\mu = 0$, left) and wind-on ($\mu = 0.05$, right) tests.*

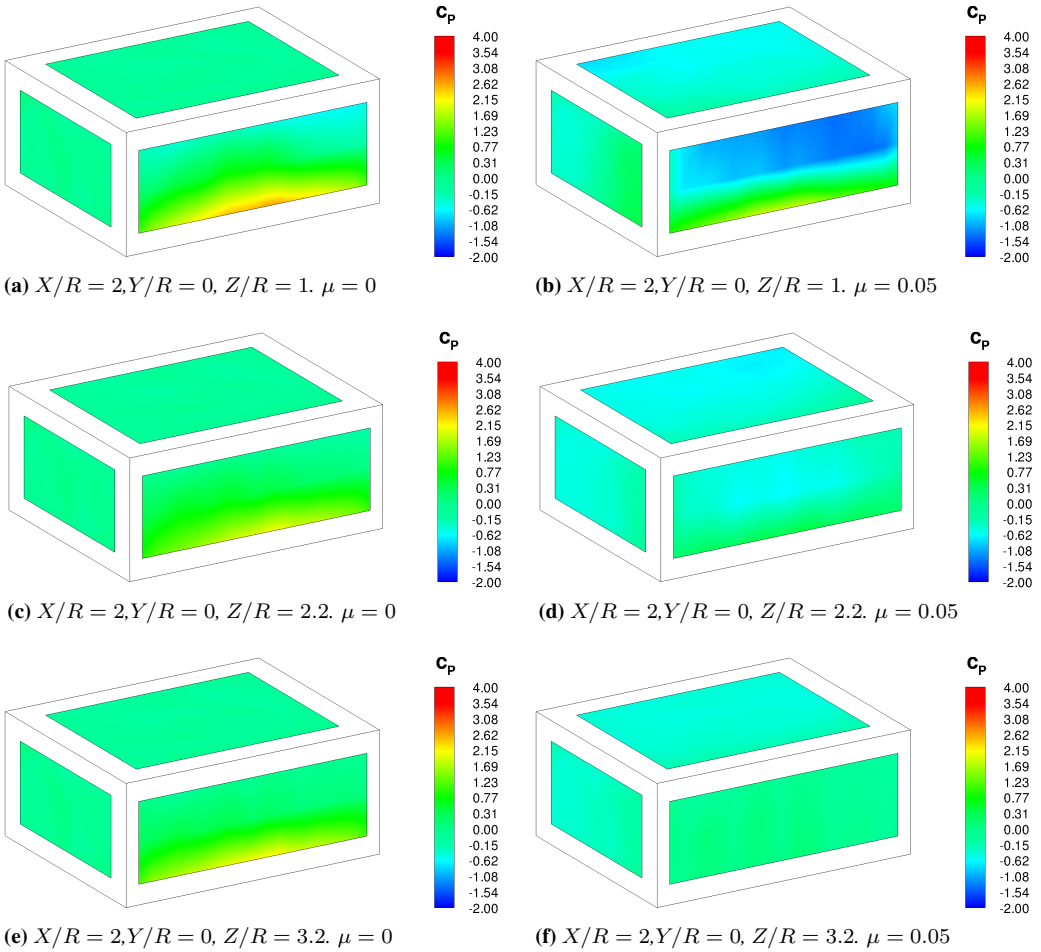

(a) $X/R = 2, Y/R = 0,\ Z/R = 1.\ \mu = 0$

(b) $X/R = 2, Y/R = 0,\ Z/R = 1.\ \mu = 0.05$

(c) $X/R = 2, Y/R = 0,\ Z/R = 2.2.\ \mu = 0$

(d) $X/R = 2, Y/R = 0,\ Z/R = 2.2.\ \mu = 0.05$

(e) $X/R = 2, Y/R = 0,\ Z/R = 3.2.\ \mu = 0$

(f) $X/R = 2, Y/R = 0,\ Z/R = 3.2.\ \mu = 0.05$

Figure 4.13: *Test T3 - Pressure coefficient contours for different helicopter heights. Comparison between wind-off ($\mu = 0$, left) and wind-on ($\mu = 0.05$, right) tests.*

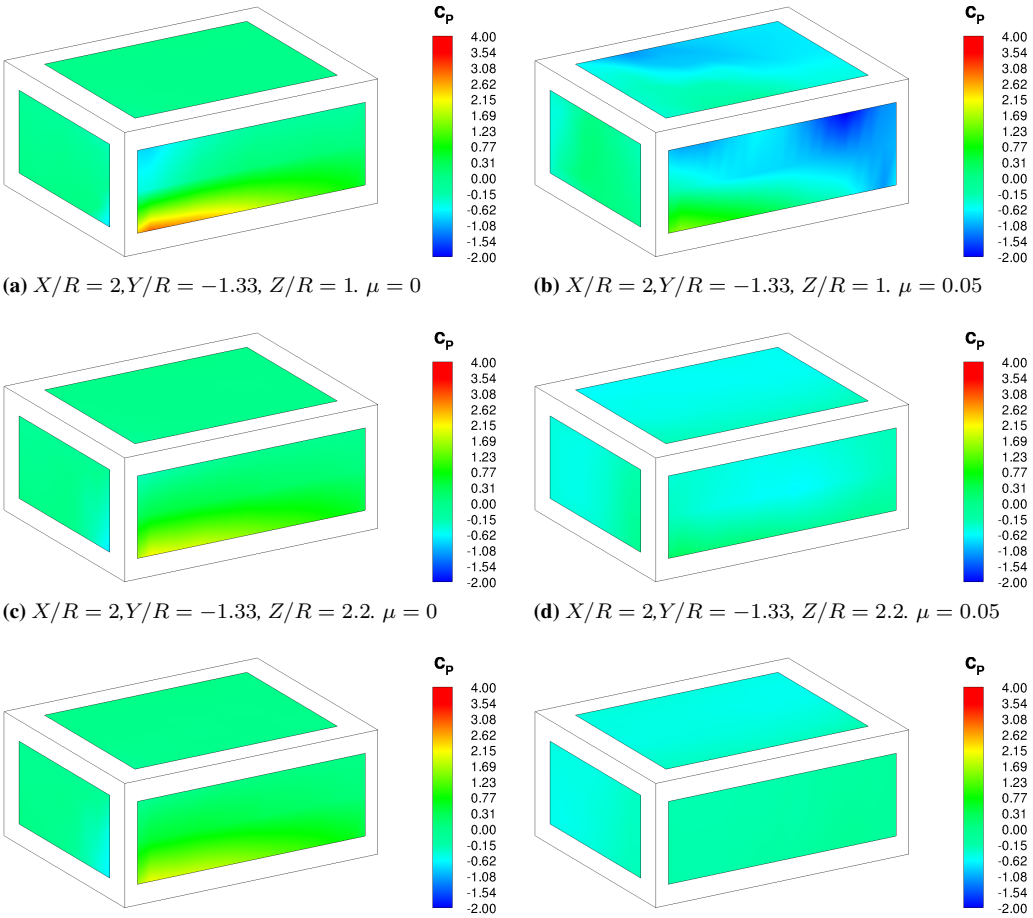

(a) $X/R = 2$,$Y/R = -1.33$, $Z/R = 1.$ $\mu = 0$

(b) $X/R = 2$,$Y/R = -1.33$, $Z/R = 1.$ $\mu = 0.05$

(c) $X/R = 2$,$Y/R = -1.33$, $Z/R = 2.2.$ $\mu = 0$

(d) $X/R = 2$,$Y/R = -1.33$, $Z/R = 2.2.$ $\mu = 0.05$

(e) $X/R = 2$,$Y/R = -1.33$, $Z/R = 3.2.$ $\mu = 0$

(f) $X/R = 2$,$Y/R = -1.33$, $Z/R = 3.2.$ $\mu = 0.05$

Figure 4.14: *Test T4 - Pressure coefficient contours for different helicopter heights. Comparison between wind-off ($\mu = 0$, left) and wind-on ($\mu = 0.05$, right) tests.*

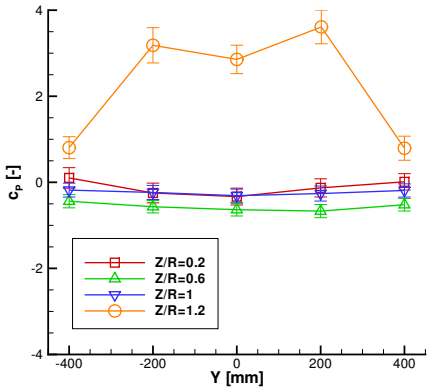

(a) *Rotor at* $X/R = -1, Y/R = 0,\ Z/R = 2.$ $\mu = 0$

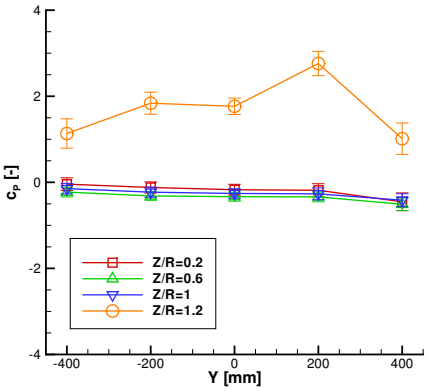

(b) *Rotor at* $X/R = -1, Y/R = 0,\ Z/R = 2.$ $\mu = 0.05$

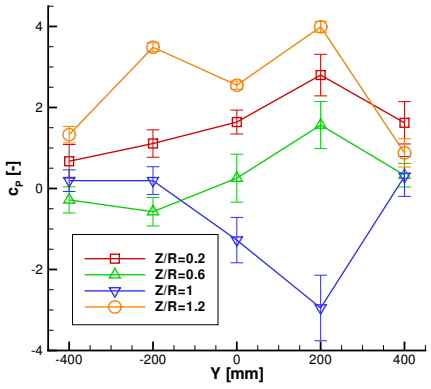

(c) *Rotor at* $X/R = 0, Y/R = 0,\ Z/R = 2.$ $\mu = 0$

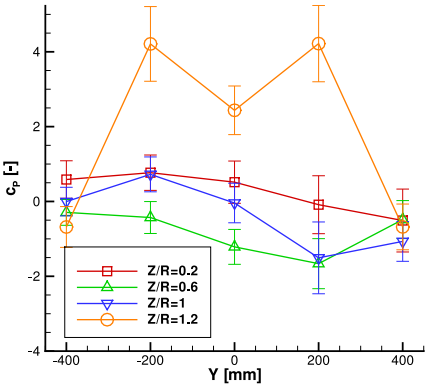

(d) *Rotor at* $X/R = 0, Y/R = 0,\ Z/R = 2.$ $\mu = 0.05$

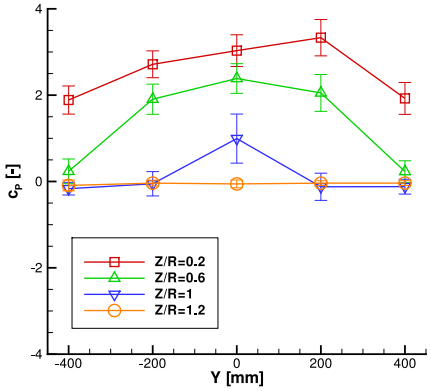

(e) *Rotor at* $X/R = 1, Y/R = 0,\ Z/R = 2.$ $\mu = 0$

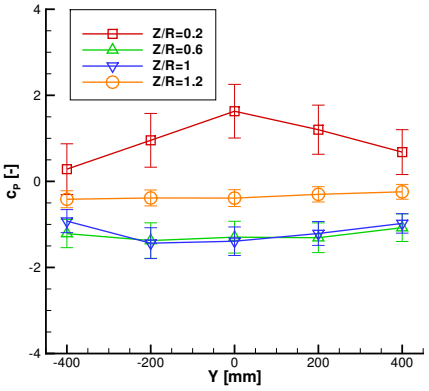

(f) *Rotor at Rotor at* $X/R = 1, Y/R = 0,\ Z/R = 2.$ $\mu = 0.05$

Figure 4.15: *Test T2 - Averaged pressure coefficient and standard deviation of the pressure coefficient (represented as error bar) measured by the Kulite transducers for various rotor positions. Comparison between wind-off* ($\mu = 0$, *left) and wind-on* ($\mu = 0.05$, *right) tests.*

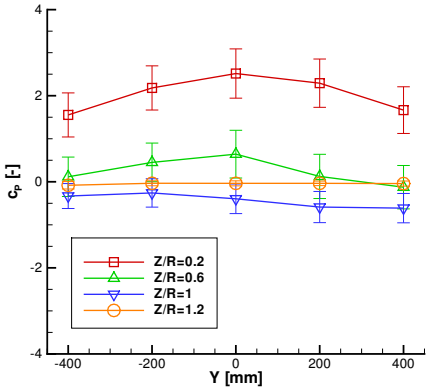

(a) *Rotor at* $X/R = 2, Y/R = 0,\ Z/R = 1.$ $\mu = 0$

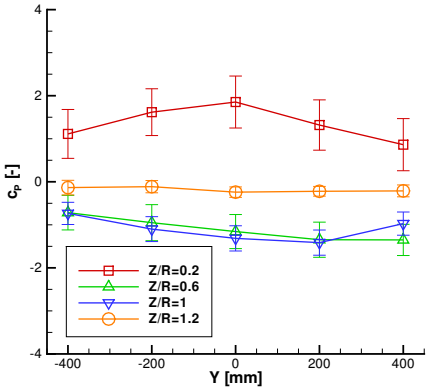

(b) *Rotor at* $X/R = 2, Y/R = 0,\ Z/R = 1.$ $\mu = 0.05$

Figure 4.16: *Test T3 - Averaged pressure coefficient and standard deviation of the pressure coefficient (represented as error bar) measured by the Kulite transducers. Comparison between wind-off* ($\mu = 0$, *left) and wind-on* ($\mu = 0.05$, *right) tests.*

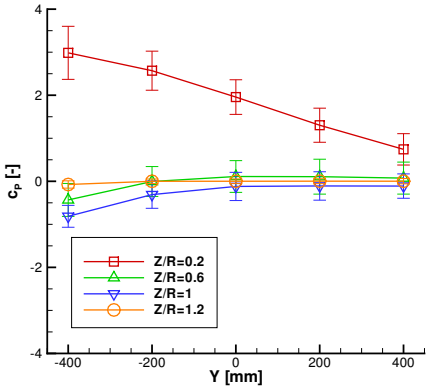

(a) *Rotor at* $X/R = 2, Y/R = -1.33,\ Z/R = 1.$ $\mu = 0$

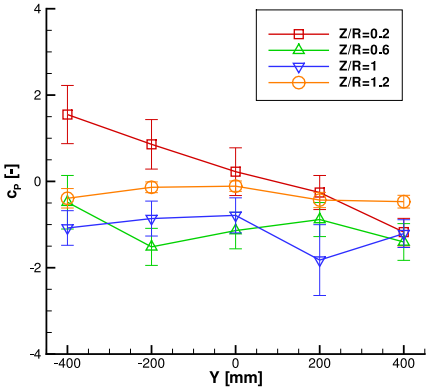

(b) *Rotor at* $X/R = 2, Y/R = -1.33,\ Z/R = 1.$ $\mu = 0.05$

Figure 4.17: *Test T4 - Averaged pressure coefficient and standard deviation of the pressure coefficient (represented as error bar) measured by the Kulite transducers. Comparison between wind-off* ($\mu = 0$, *left) and wind-on* ($\mu = 0.05$, *right) tests.*

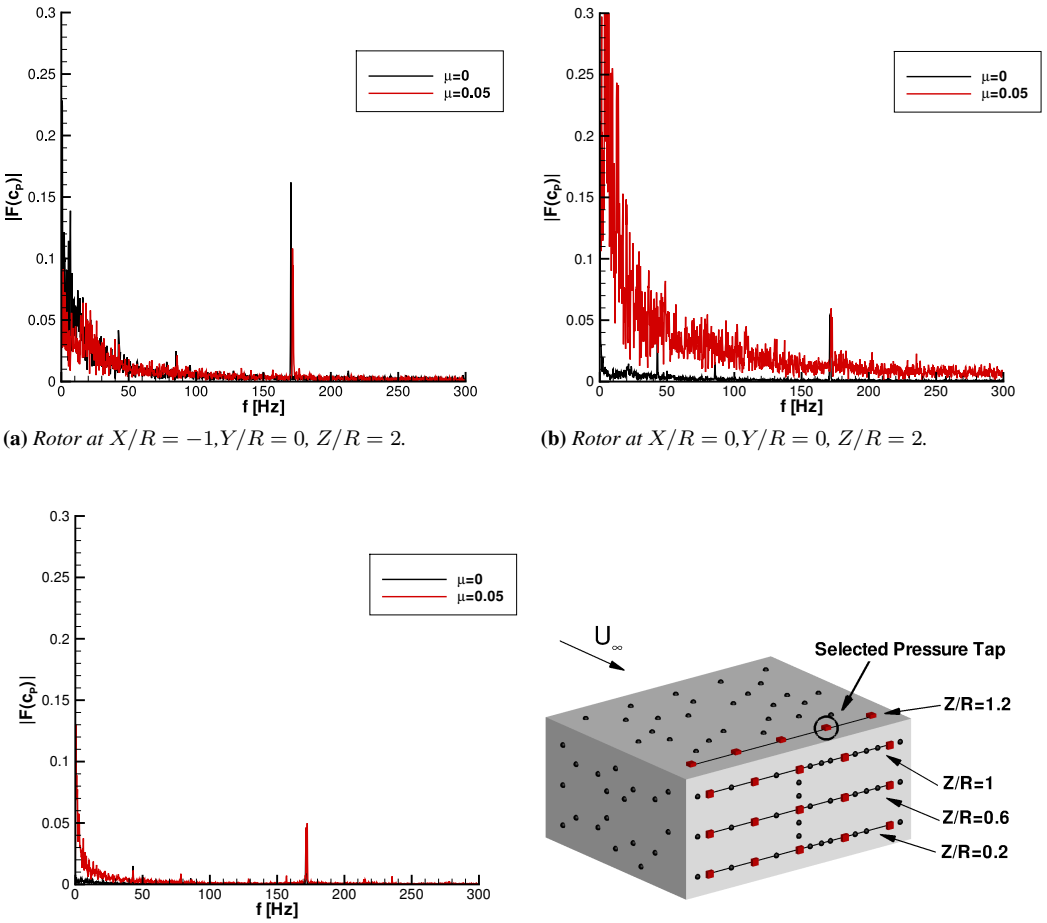

(a) *Rotor at* $X/R = -1, Y/R = 0,\ Z/R = 2.$

(b) *Rotor at* $X/R = 0, Y/R = 0,\ Z/R = 2.$

(c) *Rotor at* $X/R = 1, Y/R = 0,\ Z/R = 2.$

(d) *Selected Kulite for Fourier Analysis. Tap positioned at* $X/R = -0.27\,,\ Y/R = 0.53,\ Z/R = 1.2.$

Figure 4.18: *Test T2 - Amplitude of the pressure coefficient Fourier Transform, Pressure tap at* $X/R = -0.27\,,\ Y/R = 0.53,\ Z/R = 1.2$ *- Comparison between wind-off and wind-on tests.*

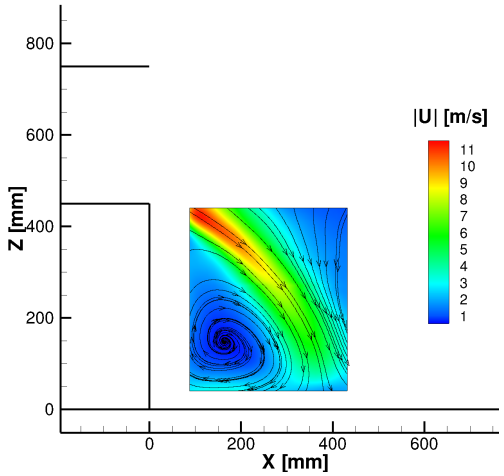

(a) $X/R = -1, Y/R = 0,\ Z/R = 2.\ \mu = 0$

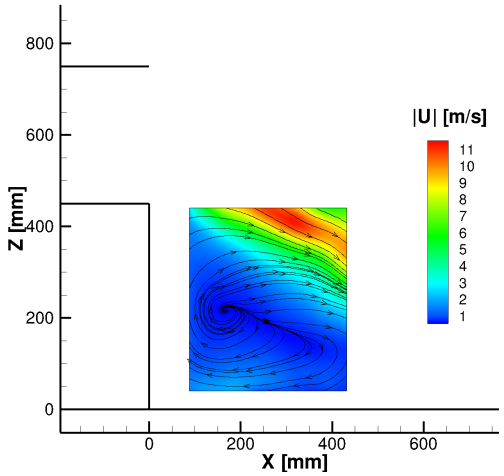

(b) $X/R = -1, Y/R = 0,\ Z/R = 2.\ \mu = 0.05$

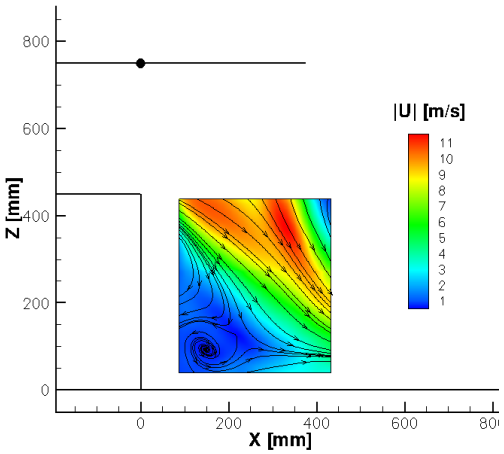

(c) $X/R = 0, Y/R = 0,\ Z/R = 2.\ \mu = 0$

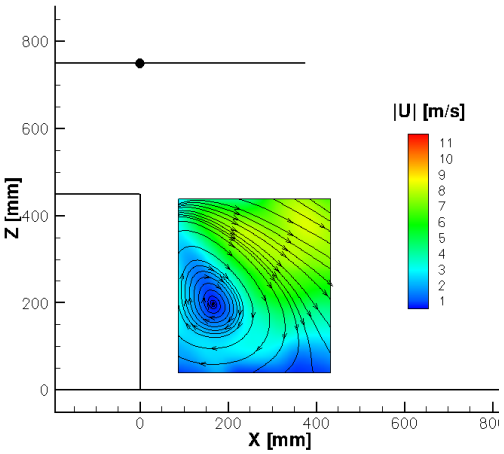

(d) $X/R = 0, Y/R = 0,\ Z/R = 2.\ \mu = 0.05$

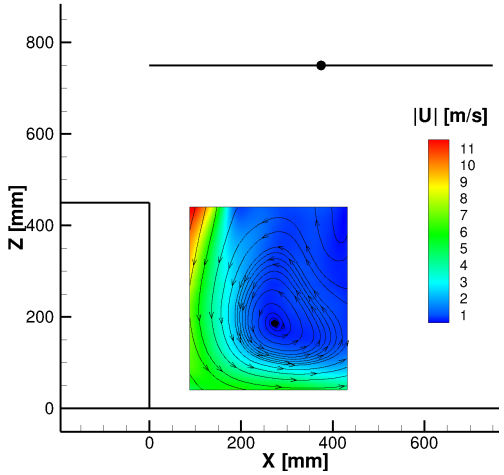

(e) $X/R = 1, Y/R = 0,\ Z/R = 2.\ \mu = 0$

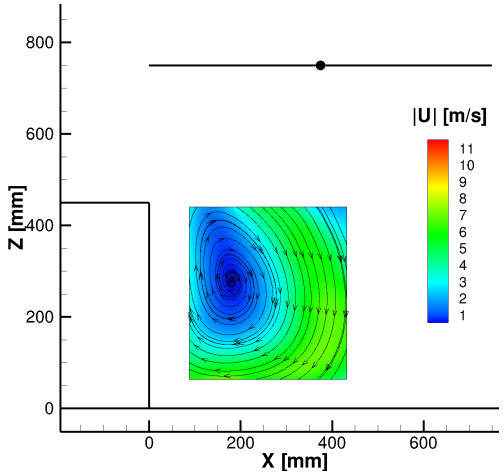

(f) $X/R = 1, Y/R = 0,\ Z/R = 2.\ \mu = 0.05$

Figure 4.19: *PIV results for test T2: In-plane velocity magnitude contours and streamlines. Comparison between wind-off ($\mu = 0$, left) and wind-on ($\mu = 0.05$, right) tests.*

CHAPTER 5

Conclusions

In the present doctoral dissertation a comprehensive experimental survey on the aerodynamic interaction between a rotor and a model ground obstacle has been described.

The experimental activities were carried out at Politecnico di Milano and University of Glasgow and took advantage of several rotor rigs and experimental techniques. Load measurements on the rotor were carried out in order to assess the rotor performance for different rotor positions with respect to the obstacle. Laser Doppler Anemometry (LDA) measurements of the rotor inflow were used in order to see how the aerodynamic interaction affected the rotor performance. Particle Image Velocimetry (PIV) measurements in the region between the rotor and the obstacle were carried out in order to have a better insight of the interacting flow field. Steady and unsteady pressure measurements on the obstacle allowed a better understanding of the loads that the helicopter creates on the surroundings.

The first activity, carried out both at the University of Glasgow and Politecnico di Milano, was the analysis or the helicopter/obstacle interaction in absence of external wind. The helicopter model was placed at different positions with respect to the obstacle thus simulating a set of possible hovering flights around the obstacle.

The investigation showed two main regions of interest. The first region is the one above the edge of the obstacle, where the helicopter experiences a gradual ground effect as it is positioned over the obstacle. In this case also a gradual reduction of the inflow velocity is observed, as prescribed by the ground effect. Since only part

of the rotor is over the obstacle, one would expect the inflow to be non-symmetrical. However, it results to be indeed symmetrical, leading to the generation of almost null pitch and roll moments.

The second region, probably of more interest, is the one just beside the obstacle where a recirculation region between the rotor and the obstacle develops. Its morphology is deeply dependent on the rotor position. This recirculation region implies a severe thrust loss (up to 8%) with respect to the one without obstacle at the same height. This thrust loss has a maximum at approximately 2 radia from the obstacle, whereas its influence appears to be negligible when the rotor is more than 4 radia away from the obstacle. Another important feature of this region is the arising of strong pitching and rolling moments (up to 30% of the measured torque), due to the non symmetrical inflow pattern on the rotor. Limited torque variations were observed throughout the testing, leading to the fact that the rotor figure of merit varied mostly according to the thrust coefficient.

When the helicopter is positioned out of the symmetry plane of the problem, the effect of the flow recirculation on the rotor performance becomes less intense, owing to the fact that only half rotor faces the obstacle. Consequently also the pitch-moment generated in this region is less intense. However, since just half of the rotor is affected by the recirculating flow, a roll moment is generated.

Despite the differences in the test rigs and test conditions adopted in the Glasgow and Milan experimental campaigns, very comparable results were obtained in terms of rotor performance, thus giving a rather strong trust in the fact that the highlighted phenomena are indeed quite general and not typical of just one configuration.

The effect of the presence of external wind was then investigated at Politecnico di Milano. A first set of measurements without the obstacle showed that the ground effect in windy conditions appears to be less intense with respect to the one without wind, and it affects the helicopter only at very low heights. Moreover, as it was appreciated for the wind-off case, the ground effect experienced by the helicopter over the obstacle is practically equivalent to the one over an infinite surface, thus highlighting the reduced influence of the obstacle wake during a landing on its upper surface.

The effect of the obstacle wake becomes definitely more relevant when the helicopter is behind the obstacle. In particular the detrimental effects caused by the recirculation region that develops for the wind-off test seems to be mitigated in windy conditions, due to the fact that the wake of the obstacle does not allow the complete development of such recirculation region. However the helicopter is affected by a severe thrust coefficient reduction when it interacts with the lateral flow structures of the obstacle wake (i.e. the horseshoe vortex), where strong velocity gradients are present.

From the point of view of the loads on the surroundings, the obstacle experiences remarkable spatial and time-variation of the pressure patterns, strongly de-

pendent on the helicopter position. High pressure regions occur on the obstacle in the regions directly underneath the rotor or in those regions where the rotor wake impinges after being deflected by the ground. These regions are usually also characterized by a fair degree of unsteadiness. When the helicopter model is placed directly over the obstacle edge, the pressure distributions on the front face of the obstacle present a diagonal pattern on the front face, probably due to the helicoidal structure of the rotor wake. This region is characterised by remarkable pressure fluctuations and the presence of contextual high and low-pressure regions. The effect of the wind on the obstacle usually leads to a reduction in the pressure peaks, even though the pressure fluctuations on the obstacle are even magnified in certain positions.

List of Figures

List of Tables

Bibliography

[1] Dooyong Lee, Nilay Sezer-Uzol, Joseph F Horn, and Lyle N Long. Simulation of helicopter shipboard launch and recovery with time-accurate airwakes. *Journal of Aircraft*, 42(2):448–461, 2005.

[2] U.S. Joint Helicopter Safety Analysis Team. The compendium report:the u.s. jhsat baseline of helicopter accident analysis. Technical report, International Helicopter Safety Team, 2011.

[3] Philip F Sheridan and Robert P Smith. Interactional aerodynamics-a new challenge to helicopter technology. *Journal of the American Helicopter Society*, 25(1):3–21, 1980.

[4] Dimitris N Mavris, Narayanan M Komerath, and Howard M McMahon. Prediction of aerodynamic rotor-airframe interactions in forward flight. *Journal of the American Helicopter Society*, 34(4):37–46, 1989.

[5] H Affes, AT Conlisk, JM Kim, and NM Komerath. Model for rotor tip vortex-airframe interaction. ii-comparison with experiment. *AIAA journal*, 31(12):2274–2282, 1993.

[6] David T Balch. Experimental study of main rotor/tail rotor/airframe interaction in hover. *Journal of the American Helicopter Society*, 30(2):49–56, 1985.

[7] G. K. Timm. Obstacleinduced flow recirculation. *Journal of the American Helicopter Society*, 10(4):5–24, 1965.

[8] Naohiro Iboshi, Noriaki Itoga, JVR Prasad, and Lakshmi N Sankar. Ground effect of a rotor hovering above a confined area. *Frontiers in Aerospace Engineering*, 3(1), 2014.

[9] SJ Zan. On aerodynamic modelling and simulation of the dynamic interface. *Proceedings of the Institution of Mechanical Engineers, Part G: Journal of Aerospace Engineering*, 219(5):393–410, 2005.

[10] SJ Zan. Experimental determination of rotor thrust in a ship airwake. *Journal of the American Helicopter Society*, 47(2):100–108, 2002.

[11] Richard G Lee and Steven J Zan. Unsteady aerodynamic loading on a helicopter fuselage in a ship airwake. *Journal of the American Helicopter Society*, 49(2):149–159, 2004.

[12] Richard G Lee and Steven J Zan. Wind tunnel testing of a helicopter fuselage and rotor in a ship airwake. *Journal of the American Helicopter Society*, 50(4):326–337, 2005.

[13] Christopher H Kääriä, Yaxing Wang, Gareth D Padfield, James S Forrest, and Ieuan Owen. Aerodynamic loading characteristics of a model-scale helicopter in a ship's airwake. *Journal of Aircraft*, 49(5):1271–1278, 2012.

[14] Christopher H Kääriä, Yaxing Wang, Mark D White, and Ieuan Owen. An experimental technique for evaluating the aerodynamic impact of ship superstructures on helicopter operations. *Ocean Engineering*, 61:97–108, 2013.

[15] TA Quinliven and KR Long. Rotor performance in the wake of a large structure. In *American Helicopter Society 65th Annual Forum*, May 2009.

[16] G. Rajagopalan, S Niazi, A.J. Wadcock, G.K.Yamauchi, and M.J. Silva. Experimental and computational study of the interaction between a tandem-rotor helicopter and a ship. In *American Helicopter Society* 61^{th} *Annual Forum*, June 1-3 2005.

[17] Yavuz Nacakli and Drew Landman. Helicopter downwash/frigate airwake interaction flowfield piv surveys in a low speed wind tunnel. In *AHS 67th annual forum*, pages 1–11, 2011.

[18] S.A. Polsky and C.H. Wilkinson. A computational study of outwash for a helicopter operating near a vertical face with comparison to experimental data. In *AIAA–2009–5684*, Chicago, IL, USA, August 10–13 2009. AIAA Modeling and Simulation Technologies Conference.

[19] C. Crozon, R. Steijl, and G.N. Barakos. Numerical study of helicopter rotors in a ship airwake. *Journal of Aircraft*, 51(6):1813–1832, 2014.

[20] C. Crozon, R. Steijl, and G.N. Barakos. Numerical study of helicopter rotors in a ship airwake. 39^{th} European Rotorcraft Forum, September 3-6 2013.

[21] SM Ruffin and JD Lee. Rotorcraft flowfield prediction accuracy and efficiency using a cartesian grid framework. *International Journal of Mathematical Models and Methods in Applied Sciences*, 3(3), 2009.

[22] Laith AJ Zori and R Ganesh Rajagopalan. Navier-stokes calculations of rotor-airframe interaction in forward flight. *Journal of the American Helicopter Society*, 40(2):57–67, 1995.

[23] Frederic Le Chuiton. Actuator disc modelling for helicopter rotors. *Aerospace Science and Technology*, 8(4):285–297, 2004.

[24] NH Wakefield, SJ Newman, and PA Wilson. Helicopter flight around a ship's' superstructure. *Proceedings of the Institution of Mechanical Engineers, Part G: Journal of Aerospace Engineering*, 216(1):13–28, 2002.

[25] CE Lynch, DT Prosser, and MJ Smith. An efficient actuating blade model for unsteady rotating system wake simulations. *Computers & Fluids*, 92:138–150, 2014.

[26] M Valentini, G. Droandi, P. Masarati, and G. Quaranta. Unsteady actuating blade model for cfd/csd analysis of a tiltrotor. In *41st European rotorcraft forum*, September 1-4 2015.

[27] Franz Durst, Adrian Melling, and James H Whitelaw. Principles and practice of laser-doppler anemometry. *NASA STI/Recon Technical Report A*, 76, 1976.

[28] Zhengji Zhang. *LDA application methods: laser Doppler anemometry for fluid dynamics*. Springer Berlin, 2010.

[29] Markus Raffel, Christian E Willert, Steven Wereley, and Jürgen Kompenhans. *Particle image velocimetry: a practical guide*. Springer, 2013.

[30] R. J. Adrian. Twenty years of particle image velocimetry. *Experiments in Fluids*, 39(2):159–169, 2005.

[31] K Pahlke. Garteur helicopter cooperative research. In *36th European rotorcraft forum*, September 7-9 2010.

[32] Ajay K Prasad. Stereoscopic particle image velocimetry. *Experiments in fluids*, 29(2):103–116, 2000.

[33] G Gibertini, L Gasparini, and A Zasso. Aerodynamic design of a civil-aeronautical low speed large wind tunnel. In *AGARD conference proceedings*, pages 6–1. AGARD, 1997.

[34] David R Polak, Werner Rehm, and Albert R George. Effects of an image plane on the tiltrotor fountain flow. *Journal of the American Helicopter Society*, 45(2):90–96, 2000.

[35] David R Polak and Albert R George. Flowfield and acoustic measurements from a model tiltrotor in hover. *Journal of aircraft*, 35(6):921–929, 1998.

[36] Ganesh Rajagopalan, Saeid Niazi, Alan J. Wadcock, Gloria K. Yamauchi, and Mark J. Silva. Experimental and computational study of the interaction between a tandem-rotor helicopter and a ship. In *American Helicopter Society 61st Annual Forum*, June 2005.

[37] J. Gordon Leishman. *Principles of Helicopter Aerodynamics*, chapter 10. Cambridge University Press, New York, NY, 2000.

[38] PIVTEC. *PIVview 2C version 3.0, User Manual*. available online at www.pivtec.com.

[39] Evan A Fradenburgh. The helicopter and the ground effect machine. *Journal of the American Helicopter Society*, 5(4):24–33, 1960.

[40] R Martinuzzi and C Tropea. The flow around surface-mounted, prismatic obstacles placed in a fully developed channel flow. *Journal of Fluids Engineering*, 115:85, 1993.

[41] Hee Chang Lim, TG Thomas, and Ian P Castro. Flow around a cube in a turbulent boundary layer: Les and experiment. *Journal of Wind Engineering and Industrial Aerodynamics*, 97(2):96–109, 2009.

[42] J Sousa. Turbulent flow around a surface-mounted obstacle using 2d-3c dpiv. *Experiments in Fluids*, 33(6):854–862, 2002.

[43] Jong-Yeon Hwang and Kyung-Soo Yang. Numerical study of vortical structures around a wall-mounted cubic obstacle in channel flow. *Physics of Fluids*, 16(7):2382–2394, 2004.

[44] Alexander Yakhot, Heping Liu, and Nikolay Nikitin. Turbulent flow around a wall-mounted cube: A direct numerical simulation. *International journal of heat and fluid flow*, 27(6):994–1009, 2006.

[45] Norberto Nigro, Germán Filippini, Gerardo Franck, Mario Storti, Jorge D'Elia, et al. Flow around a sharp-edged surface-mounted cube by large eddy simulation. 2006.

[46] A Zasso, S Giappino, S Muggiasca, and L Rosa. Optimization of the boundary layer characteristics simulated at politecnico di milano boundary layer wind tunnel in a wide scale ratio ranger. In *Proceedings of the 6th Asia-Pacific Conference on Wind Engineering*, 2005.

[47] Hermann Glauert. *On the horizontal flight of a helicopter*. HM Stationery Office, 1928.

[48] Joe W Elliott, Susan L Althoff, and Richard H Sailey. Inflow measurement made with a laser velocimeter on a helicopter model in forward flight. volume 1: Rectangular planform blades at an advance ratio of 0.15. *NASA 100545*, 1988.

[49] JG Leishman and Nai-pei Bi. Aerodynamic interactions between a rotor and a fuselage in forward flight. *Journal of the American Helicopter Society*, 35(3):22–31, 1990.